



# Trace elements in abyssal peridotite olivine record melting, thermal evolution, and melt refertilization in the oceanic upper mantle

Kuan-Yu Lin<sup>1</sup> · Jessica M. Warren<sup>1</sup> · Fred A. Davis<sup>2</sup> Received: 3 April 2023 / Accepted: 8 August 2023  
© The Author(s) 2023

## Abstract

Trace element concentrations in abyssal peridotite olivine provide insights into the formation and evolution of the oceanic lithosphere. We present olivine trace element compositions (Al, Ca, Ti, V, Cr, Mn, Co, Ni, Zn, Y, Yb) from abyssal peridotites to investigate partial melting, melt–rock interaction, and subsolidus cooling at mid-ocean ridges and intra-oceanic forearcs. We targeted 44 peridotites from fast (Hess Deep, East Pacific Rise) and ultraslow (Gakkel and Southwest Indian Ridges) spreading ridges and the Tonga trench, including 5 peridotites that contain melt veins. We found that the abundances of Ti, Mn, Co, and Zn increase, while Ni decreases in melt-veined samples relative to unveined samples, suggesting that these elements are useful tracers of melt infiltration. The abundances of Al, Ca, Cr, and V in olivine are temperature sensitive. Thermometers utilizing Al and Ca in olivine indicate temperatures of 650–1000 °C, with variations corresponding to the contrasting cooling rates the peridotites experienced in different tectonic environments. Finally, we demonstrate with a two-stage model that olivine Y and Yb abundances reflect both partial melting and subsolidus re-equilibration. Samples that record lower Al- and Ca-in-olivine temperatures experienced higher extents of diffusive Y and Yb loss during cooling. Altogether, we demonstrate that olivine trace elements document both high-temperature melting and melt–rock interaction events, as well as subsolidus cooling related to their exhumation and emplacement onto the seafloor. This makes them useful tools to study processes associated with seafloor spreading and mid-ocean ridge tectonics.

**Keywords** Abyssal peridotite · Mid-ocean ridge tectonics · Olivine chemistry · Geothermometry

## Introduction

Modern plate tectonic theory is centered around the life cycle of the oceanic lithosphere, including plate formation at mid-ocean ridges and the subsequent descent of plates back into the Earth's interior at subduction zones. Investigating the processes of oceanic lithosphere formation at

ridges is thus a fundamental aspect of plate tectonics and important for understanding how materials are extracted from the Earth's interior to form its solid outer layer. Within the oceanic lithosphere, the formation and evolution of the mantle section is of particular interest owing to its volumetric dominance, which yields strong control over the physical and chemical properties of the oceanic plate (Hirth and Kohlstedt 1996; Asimow 2002; Behn et al. 2009; Naif 2018; Cramer et al. 2019). Previous studies have demonstrated that the chemical composition of abyssal peridotites (i.e., peridotites exposed on the seafloor) provide information on lithosphere formation processes that are complementary to constraints provided by basalts (e.g., Dick et al. 1984; Johnson et al. 1990; Cannat et al. 1995; Stracke 2012; Lassiter et al. 2014; Warren 2016).

Current understanding of the peridotite record of ridge processes, including estimates of the degree of partial melting, melt–rock reaction, and thermal history, are mostly based on the compositions of spinel and clinopyroxene (Dick and Bullen 1984; Johnson et al. 1990; Seyler and Brunelli

---

Communicated by Dante Canil.

✉ Kuan-Yu Lin  
kyklin@udel.edu  
Jessica M. Warren  
warrenj@udel.edu  
Fred A. Davis  
fdavis@d.umn.edu

<sup>1</sup> Department of Earth Sciences, University of Delaware, Newark, DE, USA

<sup>2</sup> Department of Earth and Environmental Sciences, University of Minnesota Duluth, Duluth, MN, USA

2018), as well as bulk-rock compositions (Hellebrand et al. 2001; Niu 2004; Bodinier and Godard 2014). In contrast, while olivine is the most abundant mineral in the upper mantle sampled by abyssal peridotites, the systematics of their olivine trace elements have yet to be examined in detail. This is due to both the low abundance of most trace elements in olivine and to olivine commonly being the most altered phase during hydrothermal alteration (e.g., Allen and Seyfried 2003). Yet, in lithologies of great geological significance, such as refractory harzburgites and dunites, olivine is the predominant phase and clinopyroxene is rare or absent. Understanding how trace elements in olivine respond to mantle processes—such as partial melting and melt–rock interaction—should provide clues on the petrogenesis of these lithologies and the tectonic processes involved.

Studies of olivine trace elements in peridotites from other tectonic settings (De Hoog et al. 2010; Foley et al. 2013; Sanfilippo et al. 2014, 2017; Rampone et al. 2016; Su et al. 2019; Chen et al. 2020; D'Souza et al. 2020; Rooney et al. 2020; Wang et al. 2021; Demouchy and Alard 2021) have provided insights into a variety of lithosphere-forming processes and mantle dynamics. For instance, De Hoog et al. (2010) showed that Cr# (defined as molar fraction of Cr over Cr + Al) and Ti in olivine are strongly correlated with spinel Cr# and whole-rock TiO<sub>2</sub> content, respectively, both of which can be used to track the degree of melt extraction and melt–rock interaction (Niu et al. 1997; Birner et al. 2021). Foley et al. (2013) reported enrichments in olivine Ti and Ca contents, which they interpreted as recording interaction with Fe–Ti rich and carbonatite melts, respectively. Because V becomes more compatible in olivine under increasingly reducing conditions (Canil and Fedortchouk 2001), Foley et al. (2013) suggested that V/Sc ratios in peridotitic olivines may record the oxygen fugacity of original melt extraction or later melt–rock interaction. Studies have reported a gradual decrease in olivine Ni and increase in Mn contents from peridotite to dunite and troctolite in ridge-type ophiolites (Sanfilippo et al. 2014; Rampone et al. 2016). Since dunite and troctolite are products of reactions between peridotite and melts with various compositions across a range of P–T conditions (e.g., Kelemen et al. 1995; Ferrando et al. 2018), this indicates the potential of these elements for tracing melt–rock interaction in the oceanic lithosphere. Melt–rock interaction is ubiquitous in the oceanic lower crust and upper mantle (e.g., Warren 2016; Gleeson et al. 2023) and modifies the composition of melts that erupt to form mid-ocean ridge basalt (MORB) (e.g., Lissenberg and MacLeod 2016).

In this study, we present olivine trace element data for abyssal peridotites from the Gakkel Ridge, Southwest Indian Ridge (SWIR), Hess Deep on the East Pacific Rise (EPR), and the Tonga Trench (Fig. 1). We demonstrate that trace elements in abyssal peridotite olivine can be grouped based on their geochemical behavior following the classification

developed by De Hoog et al. (2010) for orogenic and xenolith peridotites. We explore the use of olivine trace elements to investigate melting, melt–rock interaction, and subsolidus redistribution during cooling. These data complement the pyroxene record of these processes and serve as a tool for constraining lithosphere formation and emplacement in pyroxene-free lithologies.

## Geological settings

The peridotites in this study were recovered from the ultra-slow spreading Gakkel and Southwest Indian ridges, Hess Deep near the fast-spreading East Pacific Rise, and the intra-oceanic Tonga trench. All these peridotites have been previously characterized for their mineral major element compositions, with a subset having been characterized for pyroxene trace element contents. A summary of these samples and associated references are provided in Table 1.

### Ultra-slow spreading ridges: the Gakkel and Southwest Indian ridges

Both the Gakkel ridge and SWIR are ultra-slow spreading ridges, with average full spreading rates of 10 mm/yr and 14 mm/yr, respectively (Vogt et al. 1979; Patriat et al. 1997; Dick et al. 2003). Ultra-slow spreading results in sparse and unevenly distributed magmatic activity (Michael et al. 2003; Dick et al. 2003). Faulting accommodates some of the spreading, leading to the exposure of mantle peridotites on the seafloor (e.g., Sauter et al. 2013).

Based on bathymetric data and relative abundances of recovered lithologies, the Gakkel ridge has been divided into three tectonomagmatic regimes (Michael et al. 2003): the Western Volcanic Zone (WVZ at 7°W–3°E), the Sparsely Magmatic Zone (SMZ at 3°E–28°E), and the Eastern Volcanic Zone (EVZ at 28°E–85°E), as shown in Fig. 1b. Most of the peridotites investigated in this study were dredged from the SMZ, except for two melt-influenced peridotites from the EVZ (Fig. 1b). Mineral major element compositions, pyroxene trace element abundances, and the extent of alteration are reported in previous studies (Warren 2016; D'Errico et al. 2016; Lynn et al. 2018; Patterson et al. 2021).

The SWIR is a much longer ridge than the Gakkel ridge, consisting of a series of spreading centers offset by transform faults (Fisher and Goodwillie 1997; Mendel et al. 1997). In this study, we focus on peridotites recovered from the Oblique and Orthogonal Segments (Fig. 1c). The Oblique Segment starts at the Shaka transform fault at 9°E and continues east for 320 km before transitioning into the Orthogonal Segment at 15°E (Standish et al. 2008). This segment continues for ~650 km east before ending at the Du Toit transform fault at 25°E (Grindlay et al. 1998). Mineral

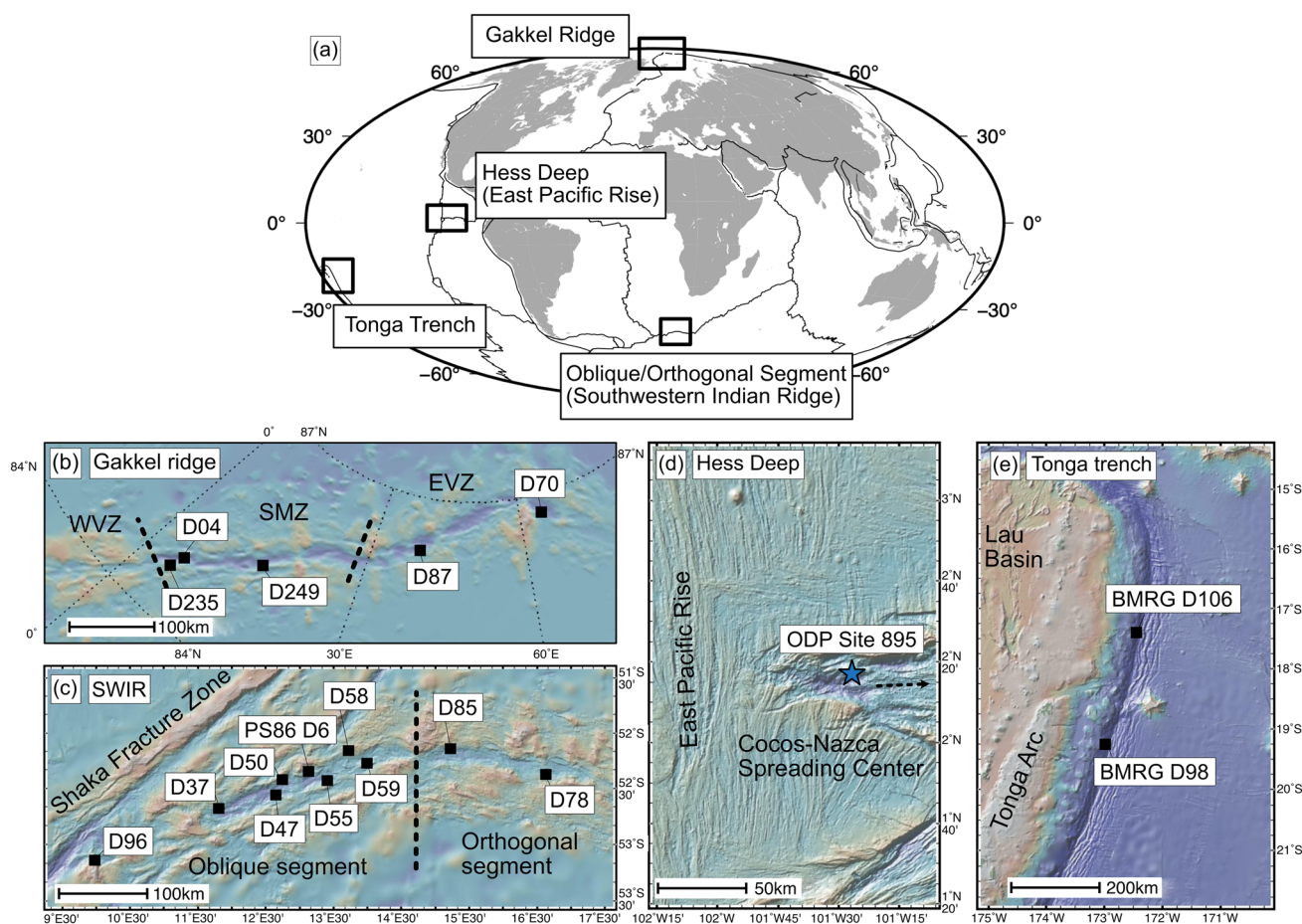


**Fig. 1** a Global map of the sample localities. Bathymetric maps are labeled with dredge and drill site locations for the **b** Gakkel ridge, **c** Oblique and Orthogonal Segments, SWIR, **d** Hess Deep, EPR and **e**

Tonga trench. The bathymetric maps were created using GeoMapApp ([www.geomapp.org](http://www.geomapp.org); Ryan et al. 2009)

major element compositions and pyroxene trace element abundances were reported in previous studies (Warren 2016; Birner et al. 2018).

### Fast spreading ridge: Hess Deep on the East Pacific Rise

Hess Deep is a 25 km long graben located at the tip of a westward propagating rift valley of the Cocos-Nazca spreading center that dissects the eastern flank of the EPR (Lonsdale 1988; Smith and Schouten 2018), which has a full spreading rate of 135 mm/yr. Hess Deep exposes basalts, sheeted dikes, lower crust, and upper mantle, which are interpreted as lithosphere created at the EPR and exposed by incipient rifting due to the Cocos-Nazca rift propagation (Fig. 1d). This environment provides a unique window into the lithosphere formed at the fast-spreading EPR axis (e.g., Karson et al. 2002; Smith et al. 2020). Samples investigated in this study are from three drill holes (A, C, and D) from ODP Leg 147, Site 895 ( $2^{\circ}16.6'$

$N$ ,  $101^{\circ}25.7' W$ ; Gillis et al. 1993), which is located south of the intra-rift crest. Mineral modes were reported in Dick and Natland (1996).

### Intra-oceanic subduction zone: the Tonga Trench

The Tonga Trench is the northern segment of the Tonga-Kermadec subduction zone in the southwest Pacific, located where the Pacific Plate subducts beneath the Indo-Australian Plate (Fig. 1e). The trench is a non-accretionary, extension-dominated convergent plate boundary (Clift 1998), which has the highest convergence rate (240 mm/yr) among subduction zones in a Pacific-fixed reference frame (Tappins et al. 1994; Bevis et al. 1995). Peridotites in this study are recovered from the nearshore flank of the trench and are lithospheric fragments from the overriding plate, which are exposed due to the lack of an accretionary prism.

Birner et al. (2017) reported mineral major elements and pyroxene trace elements and suggested that Tonga peridotite

**Table 1** Summary of peridotite samples in this study

| Sample ID                          | Petrography summary           |                               | Local geographic and tectonic summary |            |         |          |              | References <sup>c</sup> |
|------------------------------------|-------------------------------|-------------------------------|---------------------------------------|------------|---------|----------|--------------|-------------------------|
|                                    | Lithology <sup>a</sup>        | Alteration score <sup>b</sup> | Locality                              | Segment    | Lat     | Long     | Depth (mbsl) |                         |
| <i>Residual peridotites</i>        |                               |                               |                                       |            |         |          |              |                         |
| HLY0102-70-87                      | Lherz*                        | 4                             | Gakkel                                | EVZ        | 86.76°N | 64.8°E   | 3872         | 1                       |
| HLY0102-87-37                      | Harz*                         | 4                             | Gakkel                                | EVZ        | 86.34°N | 39.04°E  | 4688         | 1                       |
| PS59-235-1                         | Lherz                         | 2                             | Gakkel                                | SMZ        | 84.64°N | 4.22°E   | 4220         | 2                       |
| PS59-235-17                        | Lherz                         | 2                             | Gakkel                                | SMZ        | 84.64°N | 4.22°E   | 4220         | 2                       |
| PS59-235-18                        | Lherz                         | 2                             | Gakkel                                | SMZ        | 84.64°N | 4.22°E   | 4220         | 2                       |
| PS59-249-12                        | Harz                          | 3.5                           | Gakkel                                | SMZ        | 85.38°N | 14.73°E  | 2809         | 1                       |
| PS59-249-60                        | Harz                          | 3.5                           | Gakkel                                | SMZ        | 85.38°N | 14.73°E  | 2909         | 1                       |
| PS59-249-74                        | Harz                          | 4                             | Gakkel                                | SMZ        | 85.38°N | 14.73°E  | 2809         | 1, 3                    |
| Kn162-9-37-10                      | Harz                          | 4                             | SWIR                                  | Oblique 2  | 52.68°S | 11.81°E  | 3916         | 4                       |
| Kn162-9-37-14                      | Harz                          | 3.5                           | SWIR                                  | Oblique 2  | 52.68°S | 11.81°E  | 3916         | 4                       |
| Kn162-9-50-7                       | Lherz                         | 4                             | SWIR                                  | Oblique 2  | 52.42°S | 12.75°E  | 3930         | 4                       |
| Kn162-9-55-23                      | Lherz                         | 4.5                           | SWIR                                  | Oblique 2  | 52.43°S | 13.41°E  | 4094         | 4                       |
| Kn162-9-58-16                      | Harz                          | 4                             | SWIR                                  | Oblique 2  | 52.16°S | 13.73°E  | 2575         | 4                       |
| Kn162-9-59-2                       | Lherz                         | 3.5                           | SWIR                                  | Oblique 2  | 52.28°S | 14°E     | 3553         | 4                       |
| Kn162-9-59-7                       | Lherz                         | 4.5                           | SWIR                                  | Oblique 2  | 52.28°S | 14°E     | 3553         | 4                       |
| PS86-6-26                          | Lherz                         | 4                             | SWIR                                  | Oblique 2  | 52.35°S | 13.13°E  | 4509         | 5, 6                    |
| Van7-85-27                         | Harz                          | 4                             | SWIR                                  | Oblique 3  | 52.14°S | 15.23°E  | 4190         | 5, 7                    |
| Van7-85-30                         | Harz*                         | 3.5                           | SWIR                                  | Oblique 3  | 52.14°S | 15.23°E  | 4190         | 7                       |
| Van7-85-47                         | Lherz                         | 4                             | SWIR                                  | Oblique 3  | 52.14°S | 15.23°E  | 4190         | 7                       |
| Van7-85-49                         | Lherz*                        | 3.5                           | SWIR                                  | Oblique 3  | 52.14°S | 15.23°E  | 4190         | 7                       |
| 895A-2R-1, 7–10 cm                 | Harz                          | 3.5                           | EPR                                   | Hess Deep  | 2.28°N  | 101.45°E | 3821         | 8                       |
| 895D-2R-2, 43–46 cm                | Harz                          | 4                             | EPR                                   | Hess Deep  | 2.28°N  | 101.45°E | 3821         | 8                       |
| 895D-4R-3, 56–60 cm                | Harz                          | 3.5                           | EPR                                   | Hess Deep  | 2.28°N  | 101.45°E | 3821         | 8                       |
| 895D-5R-1, 7–11 cm                 | Harz                          | 3                             | EPR                                   | Hess Deep  | 2.28°N  | 101.45°E | 3821         | 8                       |
| BMRG08-98-1-12                     | Harz                          | 3                             | Tonga                                 |            | 19.25°S | 172.94°W | 8194         | 9                       |
| BMRG08-98-2-7                      | Harz                          | 2                             | Tonga                                 |            | 19.25°S | 172.94°W | 8194         | 9                       |
| BMRG08-98-2-8                      | Harz                          | 1.5                           | Tonga                                 |            | 19.25°S | 172.94°W | 8194         | 9                       |
| BMRG08-98-2-18                     | Harz                          | 1.5                           | Tonga                                 |            | 19.25°S | 172.94°W | 8194         | 9                       |
| BMRG08-98-2-23                     | Harz                          | 1.5                           | Tonga                                 |            | 19.25°S | 172.94°W | 8194         | 9                       |
| BMRG08-98-2-25                     | Harz                          | 1.5                           | Tonga                                 |            | 19.25°S | 172.94°W | 8194         | 9                       |
| <i>Melt-influenced peridotites</i> |                               |                               |                                       |            |         |          |              |                         |
| HLY0102-04-63                      | Plag harz <sup>†</sup>        | 4                             | Gakkel                                | SMZ        | 84.82°N | 4.71°E   | 4294         | 1                       |
| Kn162-9-58-30                      | Plag lherz <sup>†</sup>       | 4                             | SWIR                                  | Oblique 2  | 52.16°S | 13.73°E  | 2575         | 4                       |
| PS86-6-39                          | Lherz                         | 4                             | SWIR                                  | Oblique 2  | 52.35°S | 13.13°E  | 4509         | 5, 4                    |
| Van7-78-40                         | Plag harz <sup>†</sup>        | 4                             | SWIR                                  | Orthogonal | 52.38°S | 16.63°E  | 3901         | 4                       |
| Van7-96-28                         | Plag lherz <sup>†</sup>       | 4                             | SWIR                                  | Oblique 1  | 53.14°S | 9.98°E   | 3134         | 7                       |
| BMRG08-106-1-2                     | Harz <sup>†</sup>             | 3.5                           | Tonga                                 |            | 17.42°S | 172.41°W | 7423         | 9                       |
| BMRG08-106-1-5                     | Harz <sup>†</sup>             | 3.5                           | Tonga                                 |            | 17.42°S | 172.41°W | 7423         | 9                       |
| BMRG08-106-1-15                    | Dunite                        | 2.5                           | Tonga                                 |            | 17.42°S | 172.41°W | 7423         | 9                       |
| BMRG08-106-1-17                    | Harz <sup>†</sup>             | 3                             | Tonga                                 |            | 17.42°S | 172.41°W | 7423         | 9                       |
| <i>Melt-veined peridotites</i>     |                               |                               |                                       |            |         |          |              |                         |
| PS59-235-04                        | Ol websterite                 | 1.5                           | Gakkel                                | SMZ        | 84.64°N | 4.22°E   | 4220         | 3                       |
| Van7-78-25                         | Dunite with gabbro vein       | 2.5                           | SWIR                                  | Orthogonal | 52.38°S | 16.63°E  | 3901         | 4                       |
| Van7-78-31M                        | Plag peridotite w/gabbro vein | 3.5                           | SWIR                                  | Orthogonal | 52.38°S | 16.63°E  | 3901         | 4                       |
| Van7-78-36A                        | Plag peridotite w/gabbro vein | 4                             | SWIR                                  | Orthogonal | 52.38°S | 16.63°E  | 3901         | 4                       |
| Van7-78-36B                        | Plag peridotite w/gabbro vein | 4                             | SWIR                                  | Orthogonal | 52.38°S | 16.63°E  | 3901         | 4                       |

<sup>a</sup>Lithology: samples with an asterisk (\*) contain trace amount of plagioclase but are not enriched in other geochemical indices and are classified as residual in this study (see “[Sample classification and petrography](#)” section). <sup>†</sup>Interstitial plagioclase and/or clinopyroxene present

<sup>b</sup>Alteration score using the scale of Birner et al. (2016), where 1 = fresh and 5 = completely altered. For melt-veined samples, the alteration score refers to the peridotite matrix

**Table 1** (continued)

<sup>c</sup>References: 1=Lynn et al. (2018); 2=D'Errico et al. (2016); 3=Hellebrand et al. (2005); 4=Birner et al. (2021); 5=Warren (2007); 6=Salters and Dick (2002); 7=Warren et al. (2009); 8=Dick and Natland (1996); 9=Birner et al. (2017)

compositions are best explained as residues of melting during subduction initiation and formation of the forearc crust. A subset of samples from one dredge (D106) shows evidence for flux melting (Birner et al. 2017).

## Sample classification and petrography

Samples in this study have experienced hydrothermal alteration and are described in Table 1 using the alteration scores developed by Birner et al. (2016). On average, peridotites from SWIR and Hess Deep are more altered than those from Gakkal and Tonga, which include some of the freshest abyssal peridotites ever recovered (Birner et al. 2016; D'Errico et al. 2016; Patterson et al. 2021). As the composition of mantle minerals remaining after hydrothermal alteration are unmodified, even when only small islands of minerals remain within the serpentine matrix (Birner et al. 2016), we use these minerals to explore the high-temperature history of our samples.

We classified samples in this study as residual, melt-influenced, and melt-veined peridotites based on petrographic and geochemical criteria (Table 1). Samples that contain veins are straightforward to classify, whereas those without petrographically identifiable veins are classified into either residual peridotites or melt-influenced peridotites based on their spinel TiO<sub>2</sub> content and their normalized clinopyroxene Ce/Yb ratio (Fig. 2).

- Residual peridotites have spinel TiO<sub>2</sub> < 0.1 wt% and (Ce/Yb)<sub>N</sub> < 0.08 (Fig. 2a, b). They have a typical upper mantle assemblage of olivine, orthopyroxene, clinopyroxene, and spinel, with compositions that reflect various degrees of melt extraction. In this study, residual peridotites have either protogranular (Fig. 3a) or porphyroclastic (Fig. 3b) textures. Residual peridotites are further subcategorized into lherzolites and harzburgites based on whether they have > 5% or < 5% modal clinopyroxene, respectively (Le Maitre et al. 2002).
- Melt-influenced peridotites have spinel TiO<sub>2</sub> > 0.1 wt% and/or (Ce/Yb)<sub>N</sub> > 0.08 (Fig. 2a, b). The elevated (Ce/Yb)<sub>N</sub> ratios correspond to light rare earth element (LREE)-enriched patterns (Fig. 2c, d). Petrographically, most of the melt-influenced peridotites contain either plagioclase (commonly altered) or interstitial clinopyroxene (e.g., Seyler et al. 2001; Fig. 3c, d).
- Samples with identifiable veins in thin sections and hand samples are classified as melt-veined peridotites (Fig. 3e,

f). These samples always meet our criteria for melt-influenced samples, which supports our application of spinel TiO<sub>2</sub> content and clinopyroxene (Ce/Yb)<sub>N</sub> as indicators of interaction with melt.

Our classification system is based on previous studies on these samples (Warren 2016; D'Errico et al. 2016; Birner et al. 2018, 2021). Despite the interpretive component in “residual” and “melt-influenced” terminology, we consider them the best ones that can account for the geochemical characteristics of these rocks compared to alternative terminologies, such as “depleted/enriched”, “refractory/fertile”, or “metasomatized”, which have specific geochemical implications (e.g., Byerly and Lassiter 2014).

The collection of SWIR peridotites in this study includes 12 residual, 4 melt-influenced, and 4 melt-veined samples. The residual peridotites comprise 7 lherzolites and 5 harzburgites (Table 1). The SWIR melt-veined peridotites are from dredge Van7-78 and contain gabbroic veins (Figs. 2f, 3e). Samples from the Gakkal ridge consist of 8 residual peridotites (4 lherzolites, 4 harzburgites), 1 melt-influenced harzburgite, and 1 melt-veined peridotite. At Hess Deep, all 4 peridotites are residual harzburgites. Samples from the Tonga trench in this study include 6 residual harzburgites and 4 melt-influenced peridotites, one of which is a dunite.

## Methods

Laser ablation analyses were performed at the University of Delaware using a Thermo Scientific iCAP-TQ-ICPMS in combination with a Teledyne Analyte Excite Laser Ablation System, which has a 193 nm ArF excimer laser. We analyzed trace elements in olivine for all the samples listed in Table 1, with data compiled in Tables S1-S6. In addition, we measured trace elements in orthopyroxene (22 samples) and clinopyroxene (5 samples) in samples that had no prior pyroxene data. Here, we summarize our methodology, with further details provided in Supplementary Material A.

For olivine analyses, a spot size of 85 μm was selected with a repetition rate of 10 Hz, laser fluency = 11 J/cm<sup>2</sup>, and ~40 s ablation time. For pyroxenes, we chose a slightly larger spot size of 110 μm, repetition rate of 8 Hz and laser fluency = 12.37 J/cm<sup>2</sup>. For olivine, we measured the isotopes <sup>26</sup>Mg, <sup>27</sup>Al, <sup>29</sup>Si, <sup>44</sup>Ca, <sup>48</sup>Ti, <sup>51</sup>V, <sup>53</sup>Cr, <sup>55</sup>Mn, <sup>57</sup>Fe, <sup>59</sup>Co, <sup>60</sup>Ni, <sup>66</sup>Zn, <sup>89</sup>Y, and <sup>172</sup>Yb, with <sup>26</sup>Mg as the internal standard. For pyroxenes, we additionally measured the isotopes <sup>63</sup>Cu,

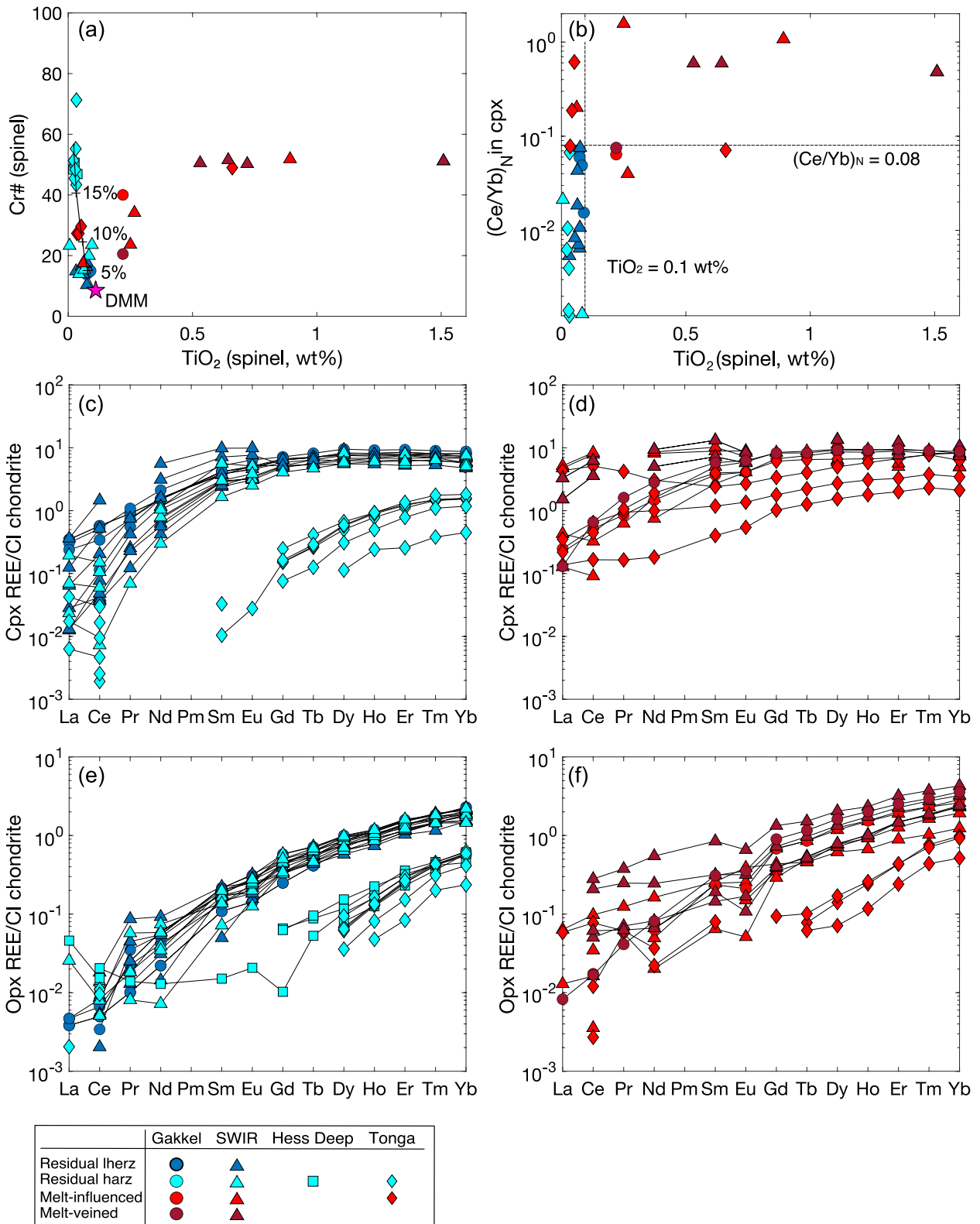


**Fig. 2** Spinel major element and pyroxene REE chemistry. **a** Spinel Cr# against TiO<sub>2</sub> content. The solid curve is the calculated spinel Ti content for a non-modal fractional melting model (parameters given in “Partial melting and sub-solidus redistribution: Ti, Y, and Yb” section) against the empirical relationship for Cr# as a function of degree of melting from Hellebrand et al. (2001). Purple star is the Depleted MORB Mantle (DMM) composition of Workman and Hart (2005). **b** Normalized cpx Ce/Yb against spinel TiO<sub>2</sub> contents for sample classification. REE variation diagrams for **c** cpx in residual peridotites, **d** cpx in melt-influenced and melt-veined peridotites, **e** opx in residual peridotites, and **f** opx in melt-influenced and melt-veined samples. Data are a combination of literature values (Warren 2007; Warren et al. 2009; D’Errico et al. 2016; Birner et al. 2017) and data from this study. All REE concentrations are normalized to chondrite (Anders and Grevesse 1989)

<sup>85</sup>Rb, <sup>88</sup>Sr, <sup>90</sup>Zr, <sup>93</sup>Nb, <sup>137</sup>Ba, <sup>139</sup>La, <sup>140</sup>Ce, <sup>141</sup>Pr, <sup>146</sup>Nd, <sup>147</sup>Sm, <sup>151</sup>Eu, <sup>159</sup>Tb, <sup>160</sup>Gd, <sup>163</sup>Dy, <sup>165</sup>Ho, <sup>166</sup>Er, <sup>169</sup>Tm, <sup>175</sup>Lu, <sup>178</sup>Hf, <sup>208</sup>Pb, and <sup>232</sup>Th. Dwell times were set to 0.05 s for <sup>26</sup>Mg, <sup>29</sup>Si, <sup>53</sup>Cr, <sup>55</sup>Mn, <sup>57</sup>Fe, <sup>59</sup>Co, <sup>60</sup>Ni, <sup>66</sup>Zn, 0.1 s for <sup>51</sup>V, and 0.5 s for all other elements to improve counting statistics at lower concentrations. Background signals were collected for approximately 8 s ahead of each ablation. The signal for each element during ablation was carefully checked. Cycles with time-resolved signals indicative of spinel inclusions (anomalous spikes of Al, Cr, V) or penetration into a different grain (sudden increase/decrease of signal) were removed (Fig. S1), as discussed further in Supplementary Material A.

Element concentrations were calculated from measured signals in counts per second using working curves constructed by measuring a mixture of MPI–DING reference glasses (Jochum et al. 2000) and USGS basaltic glasses (Jochum et al. 2005a) with values from the GeoReM database (Jochum et al. 2005b, 2016; compiled in Table S7). We demonstrate in Supplementary Material B that matrix-dependent elemental fractionation is insignificant (< 10%) at our operating conditions, which is supported by the long-term reproducibility of MongOLSh11-2 in our study (Table S8).

All analyses were conducted on thin or thick sections. Typically 4–6 olivine grains of random distribution across each sample were analyzed with at least two spots on each grain where possible. Ablation spots were located as close to the center of exposed olivine and pyroxene grains as possible. In melt-veined peridotites, all olivine and pyroxene analyses were conducted on those within the peridotite matrix.

Data were processed using the Microsoft Excel macro spreadsheet Lasyboy written by Joel Sparks at Boston University. Individual analyses of an element were excluded if (1) they show clear spikes indicative of spinel inclusions (Fig. S1, Supplementary Material A), or (2) they were within two standard deviations of the average background signal (which defines the detection limit), or (3) if an analysis had accumulated counting errors > 50% of the counts. All remaining data were used to calculate average abundances for each sample, as no systematic spatial variations were observed at the thin

section scale. To obtain long-term reproducibility, MongOLSh11-2 was analyzed as an unknown in every session and the results are in good agreement with its reported reference values (Batanova et al. 2019), as compiled in Table S8.

## Results

We report sample-averaged trace element data for olivine in Table S1, while results from individual analytical spots are presented in Table S2. Pyroxene data sets are in Tables S3–S4, with individual analytical spots in Tables S5–S6. We briefly present the pyroxene trace element results—which agree with previous studies of these samples—before describing our new olivine trace element data set for abyssal peridotites.

### Clinopyroxene and orthopyroxene REE composition

The REE concentrations in clinopyroxene from our samples are plotted in Fig. 2. The clinopyroxene REE patterns for Gakkel and SWIR residual peridotites (Fig. 2c) are generally LREE depleted. Harzburgites, on average, have clinopyroxene LREE slightly lower than lherzolites ( $La_N = 0.17$  for lherzolites compared to 0.10 for harzburgites). Clinopyroxene in Hess Deep peridotites was too small for analysis. Residual Tonga harzburgites have heavy REE (HREE) values an order of magnitude lower than Gakkel and SWIR samples. Clinopyroxene from melt-veined peridotites have higher REE abundances and higher LREE/HREE ratio than those from melt-influenced peridotites (Fig. 2d). Melt-influenced peridotites from Tonga have relatively flat REE patterns with slightly lower REE abundances than those from Gakkel and SWIR.

Orthopyroxene REE contents (Table S4) are lower than those in clinopyroxene from the same sample by approximately an order of magnitude (Fig. 2e, f), in agreement with partitioning data (e.g., Sun and Liang 2014). The Tonga and Hess Deep orthopyroxene have extremely depleted REE abundances with most of the MREE and LREE below detection. Orthopyroxene in melt-influenced and melt-veined peridotites from Gakkel and SWIR have smooth, LREE depleted patterns that are sub-parallel with one another. Melt-influenced peridotites from Tonga are again lower in REE abundances, with most LREE and MREE below the detection limit.

### Olivine trace elements

Olivine trace element abundances are plotted on a sample-averaged basis in Figs. 4, 5 and 6 against olivine forsterite content (Fo, defined as molar fraction of Mg over Mg + Fe). Literature data for olivine trace elements from continental xenoliths (Witt-Eickschen and O’Neill 2005; Witt-Eickschen et al. 2009; Mallmann et al. 2009; De Hoog et al. 2010; Quinn et al. 2018; Canil et al. 2021; Canil and Russell 2022) and ophiolitic peridotites

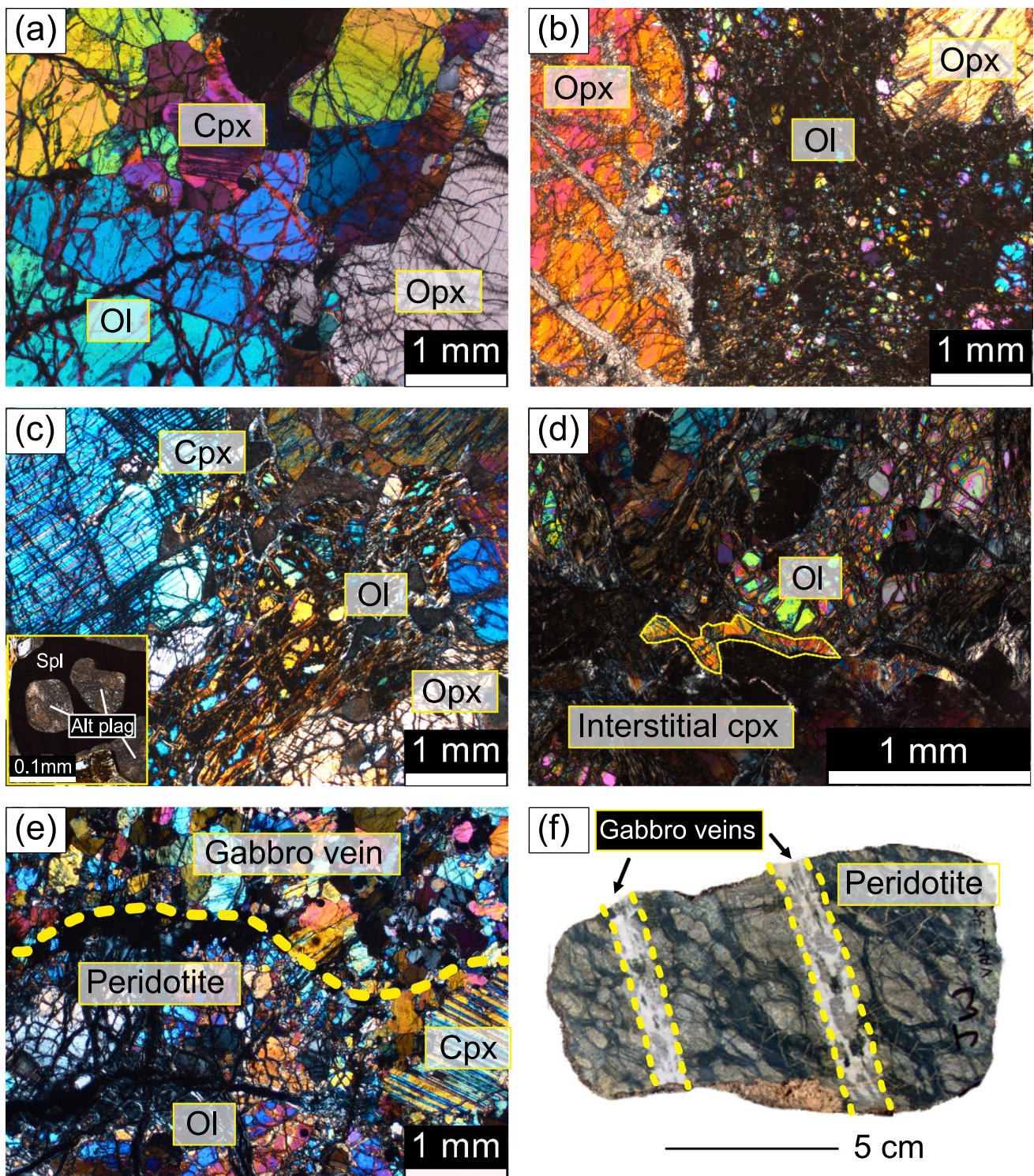


**Fig. 3** Photos of residual (a, b), melt-influenced (c, d), and melt-veined (e, f) peridotites (HLY0102-4-63). **a** Residual peridotite with protogranular texture (PS59-235-17). **b** Residual peridotite with porphyroclastic texture (Kn162-9-37-14). **c** Melt-influenced peridotite. The inset panel shows an example of spinel in this sample (not in this image) with

altered plagioclase (HLY0102-4-63). **d** Melt-influenced sample with interstitial cpx outlined in yellow (BMRG08-106-1-2). **e** Gabbro vein cross-cutting the peridotite matrix (Van7-78-25). **f** Hand specimen of a gabbro-veined peridotite (Van7-78-31). All photomicrographs are under cross-polarized light

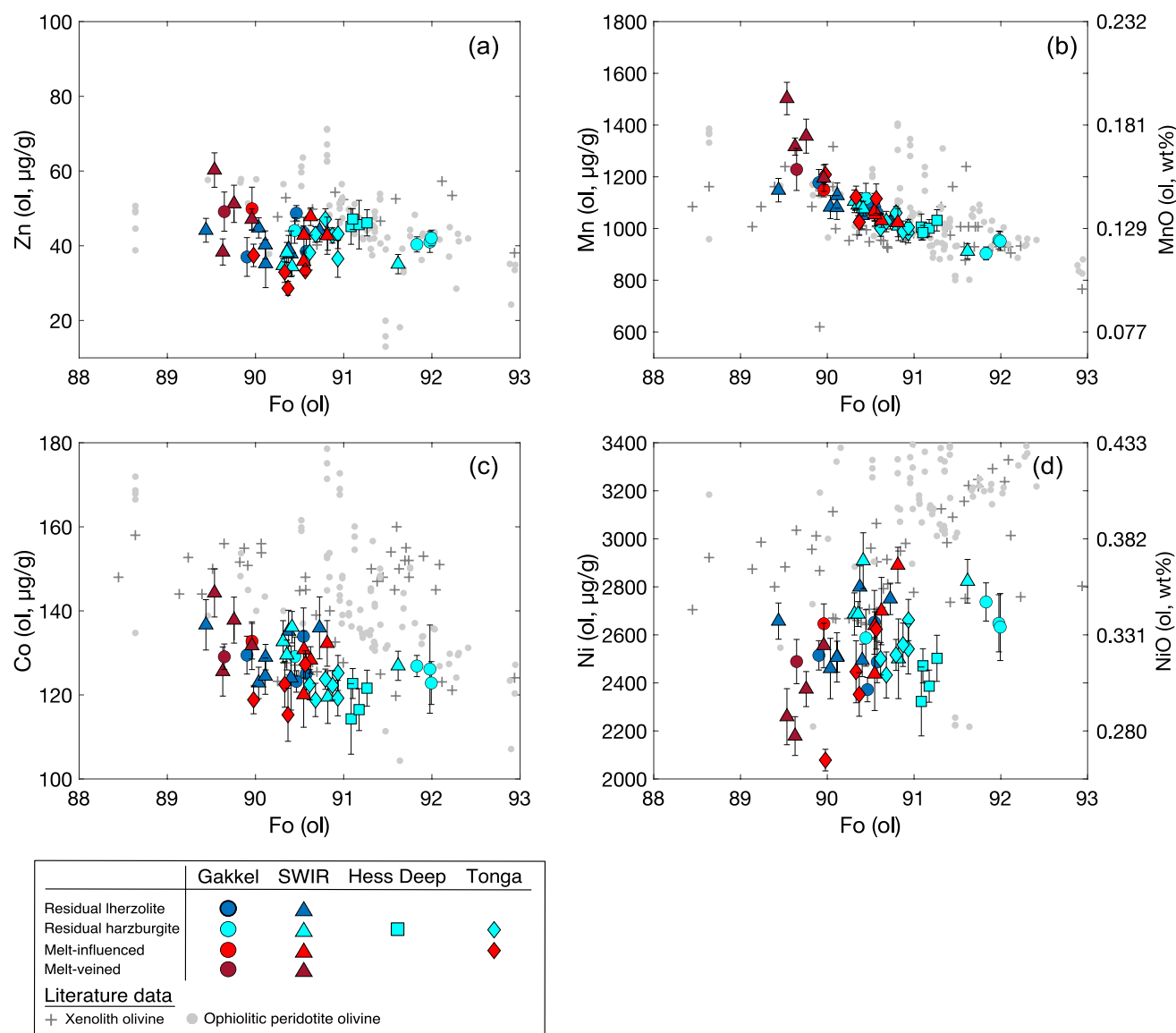


**Fig. 4** Abundances of Group I elements in olivine plotted as a function of olivine Fo content. For comparison, literature olivine data are plotted for spinel-peridotite xenoliths (Witt-Eickschen and O'Neill 2005; Witt-Eickschen et al. 2009; Mallmann et al. 2009; De Hoog

et al. 2010; Quinn et al. 2018; Canil et al. 2021; Canil and Russell 2022) and ophiolitic peridotites (Sanfilippo et al. 2014; Rampone et al. 2016; Wang et al. 2021)

(Sanfilippo et al. 2014; Rampone et al. 2016; Wang et al. 2021) are plotted in the background for comparison.

Using sample-averaged data requires evaluation of compositional heterogeneity (e.g., core–rim zonation) in olivine, which is a challenging task in abyssal peridotites due to hydrothermal alteration. For a first order evaluation, we picked a fresh peridotite from the Gakkel Ridge (PS59-235-17, alteration score 2) and collected core-to-rim transects of olivine trace elements on six different grains (Supplementary Material C). Most of the elements do not preserve systematic core-to-rim zonation. For Ti, V, and Cr, 3 out of the 6 surveyed grains contain resolvable core-to-rim zonation,

with one example illustrated in Fig. S3 and Table S9. The extent of this core–rim variability is captured by the one standard deviation obtained using only core values (Table S1 and Figs. 4, 5, 6) and does not correspond to spatial variations in composition in the sample. As the zonations in Ti, V, and Cr require further detailed analysis, the main conclusions of this study are focused on the systematics of elements that do not preserve core-to-rim zoning.

To understand the systematics of our sample-averaged olivine trace element data set, we used the groupings of De Hoog et al. (2010). Group I elements (Zn, Mn, Co, Ni) have limited concentration ranges (Fig. 4) and olivine is the

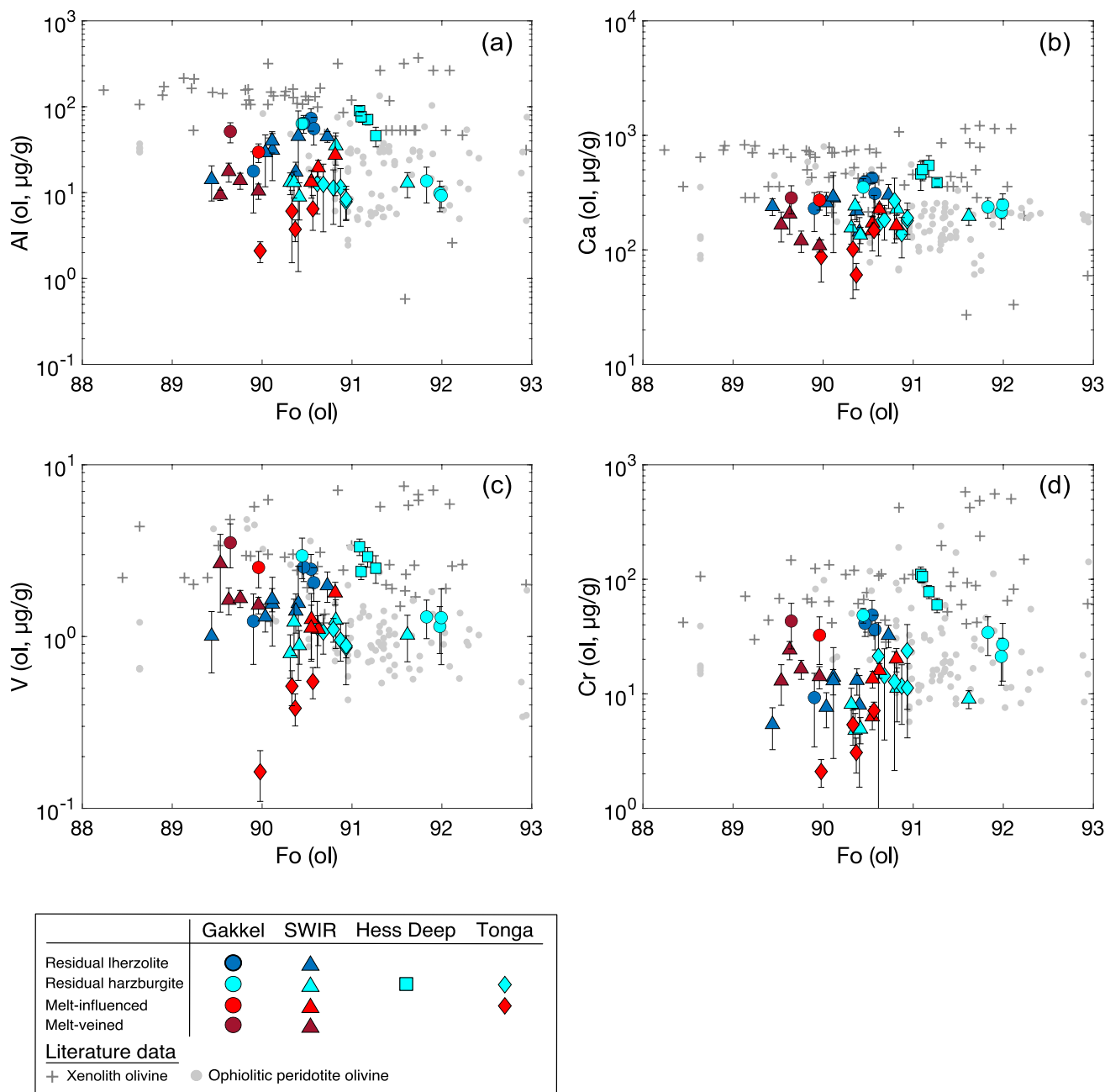


**Fig. 5** Abundances of Group II elements in olivine as a function of olivine Fo content. Literature xenolith (Witt-Eickschen and O'Neill 2005; Witt-Eickschen et al. 2009; Mallmann et al. 2009; De Hoog

et al. 2010; Quinn et al. 2018; Canil et al. 2021; Canil and Russell 2022) and ophiolitic peridotite (Sanfilippo et al. 2014; Rampone et al. 2016; Wang et al. 2021) data are plotted for comparison

dominant host of these elements in peridotites. Our abyssal peridotite olivine has Fo contents from 89.5 to 92.0, typical of upper mantle olivine, and Group I elements display a limited concentration range within this range of Fo content. Zinc and Co vary by a few tens of  $\mu\text{g/g}$ , while Mn and Ni have a slightly larger variation by a few hundred  $\mu\text{g/g}$  (Fig. 4). We find no systematic variation among these elements for the different tectonic environments of our samples. On average, the melt-veined peridotites have lower Fo

contents (89.5–90.0), lower Ni contents, and higher Mn, Co, and Zn contents than the residual peridotites (Fig. 4). The melt-influenced peridotites are intermediate in composition between melt-veined and residual harzburgites for all Group I elements. Olivine trace element data from both continental spinel peridotite xenoliths and ophiolitic peridotites have a similar abundance range to our abyssal peridotites (Fig. 4), but extend to higher abundances of Co and Ni at similar Fo contents. Group I elements, when plotted against each other

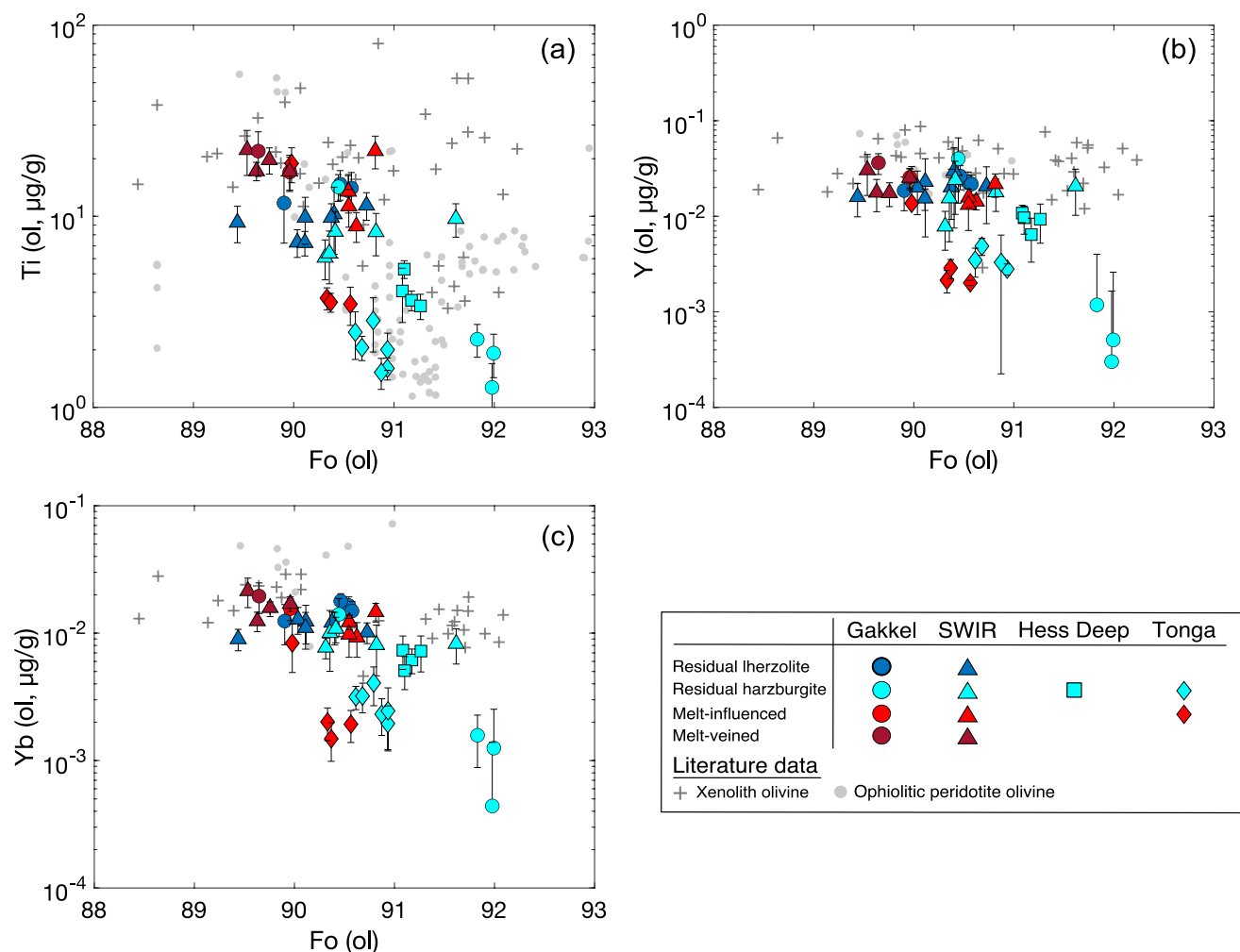


**Fig. 6** Abundances of Group III elements in olivine as a function of olivine Fo content. Literature xenolith (Witt-Eickschen and O'Neill 2005; Witt-Eickschen et al. 2009; Mallmann et al. 2009; De Hoog

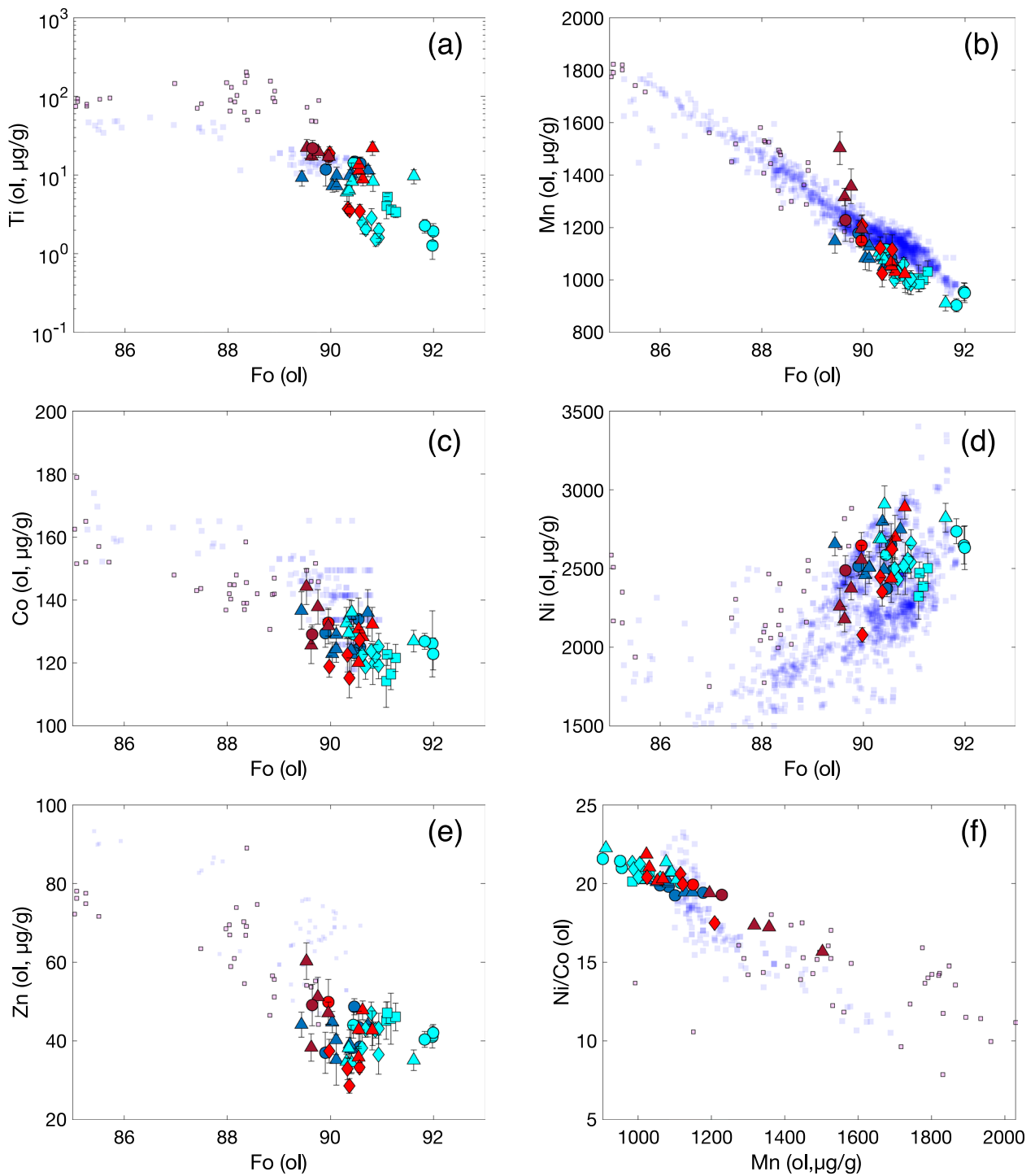
et al. 2010; Quinn et al. 2018; Canil et al. 2021; Canil and Russell 2022) and ophiolitic peridotite (Sanfilippo et al. 2014; Rampone et al. 2016; Wang et al. 2021) data are plotted for comparison

(Supplementary Material D), have statistically significant co-variations.

Group II elements (Ca, Al, V, Cr) have comparatively large concentration ranges of approximately an order of magnitude (Fig. 5). De Hoog et al. (2010) observed that the concentrations of these elements in olivine co-vary with equilibration temperatures recorded by the rock, implying a temperature dependence on their partitioning between olivine and other mantle minerals. The abundance of these elements varies among the different tectonic environments in our study (Fig. 5). Olivine in fast-spreading Hess Deep residual peridotites contains the highest abundances of Group II elements, followed by residual peridotites from the ultra-slow spreading ridges. Olivine from the Tonga trench have the lowest Group II element abundances, particularly dredge BMRG08-106 samples, which are classified here as melt-influenced peridotites. At ultra-slow spreading ridges,

both the melt-veined and melt-influenced peridotites have olivine trace element contents similar to the residual peridotites. Olivine from peridotite xenoliths have higher Group II element abundances, while ophiolitic peridotite olivine overlaps with those of our abyssal peridotites (Fig. 5).

For Group III elements, we analyzed Ti and Y, and included Yb due to its similar geochemical behavior with Y (Fig. 6). Olivine is a minor host of these elements, which are incompatible in all peridotite phases, and their abundances are controlled by partial melting (De Hoog et al. 2010) and likely subsolidus re-equilibration (Sun and Liang 2014; Cherniak and Liang 2014). The Group III elements (Fig. 6) all show general trends of decreasing abundances as Fo content increases, with variations among the different tectonic settings. Olivine from Tonga have similar Fo contents as the SWIR peridotites but have lower concentrations of Group III elements by approximately an order of magnitude.



|                        | Gakkel | SWIR | Hess Deep | Tonga |
|------------------------|--------|------|-----------|-------|
| Residual lherzolite    | ●      | ▲    |           | ◆     |
| Residual harzburgite   | ●      | ▲    | ■         | ◆     |
| Melt-influenced        | ●      | ▲    |           | ◆     |
| Melt-veined            | ●      | ▲    |           | ◆     |
| <b>Literature data</b> |        |      |           |       |
| MORB olivine           | □      |      |           |       |
| Troctolite             | □      |      |           |       |

**Fig. 7** Variation of olivine Group I elements (Mn, Co, Ni, Zn) plus Ti as a function of olivine Fo content. For comparison, literature data are plotted for troctolites (Sanfilippo et al. 2014; Rampone et al. 2016; Basch et al. 2018, 2021), and MORB olivine phenocrysts (Sobolev et al. 2007; Neave et al. 2018)

Melt-veined peridotites have higher Ti abundances than do melt-influenced and residual peridotites. When compared to olivine trace elements from xenoliths, abyssal peridotites have lower Ti, but similar Y and Yb at a given Fo content. Ophiolitic peridotite olivine mostly overlap in Ti contents when compared with our abyssal data set, while little data exist for Y and Yb in ophiolitic olivine.

## Discussion

Partial melting and melt extraction at MORs control the formation of the oceanic lithosphere during seafloor spreading (e.g., Klein and Langmuir 1987; Katz et al. 2022). Below we demonstrate that Group I element abundances in olivine are modified during melt infiltration. We then use Group II elements to evaluate the cooling history of peridotites down to temperatures lower than those recorded by pyroxene-based thermometers. Finally, we explore how Group III elements in abyssal peridotite olivine reflect a combination of partial melting followed by subsolidus re-equilibration.

### Olivine trace elements as tracers of melt–rock interaction

Reactions between percolating melts and the surrounding mantle are ubiquitous at mid-ocean ridges, influencing the compositional evolution of the oceanic lithosphere (e.g., Constantin et al. 1995; Lissenberg and Dick 2008; Drouin et al. 2009; Dick et al. 2010; Warren 2016; Zhang et al. 2021). Because olivine is present in mantle peridotites and portions of the lower oceanic crust, their trace element compositions can be useful tracers of melt evolution during various stages of melt–rock reaction, melt assimilation, and fractional crystallization (Coogan 2014; Sanfilippo et al. 2014, 2017; Rampone et al. 2016; Basch et al. 2018). In Fig. 7, we plot the variation of olivine Group I elements (Mn, Co, Ni, Zn) and Ti for samples in this study. All residual peridotites have Ni/Co ratios  $> 19$  and Mn  $< 1200$  ppm, whereas our melt-veined peridotites have Ni/Co  $< 19$  and Mn  $> 1200$  ppm (Fig. 7f). Our melt-influenced peridotites have abundances that are mostly between the melt-veined and residual harzburgites, overlapping with the residual lherzolites. This suggests that small amounts of melt–rock interaction may slightly refertilize residual harzburgites but does not significantly affect the olivine composition.

Formation of the lower oceanic crust involves melt assimilation and fractional crystallization (Coogan 2014), leading to lithologies formed across a range of melt–rock ratios. Residual peridotites are interpreted as residual mantle that has undergone limited interaction with melt, while troctolites require melt impregnation at high melt–rock ratios (e.g., Drouin et al. 2009; Sanfilippo et al. 2014; Basch et al. 2019). In Fig. 7, we compare our olivine trace element data set to those of MORB phenocrysts (Sobolev et al. 2007; Neave et al. 2018), representing an end-member of olivine precipitated from fully aggregated melts, and melt-hybridized troctolites (Rampone et al. 2016; Basch et al. 2018, 2021; Ferrando et al. 2018), which contain olivine from a rock formed at a high melt–rock ratio. Figure 7 illustrates that as melt increasingly dominates the system from residual to melt-veined peridotites to hybridized troctolites and MORB phenocrysts, olivine trends towards lower Fo, Ni, and Ni/Co contents and higher Ti, Mn, Co, and Zn contents. These observations imply that the abundance of Group I elements in olivine vary as a function of the extent of melt–rock reaction in the oceanic upper mantle and lower crust, making them potential tracers of melt addition in the oceanic lithosphere.

### Evaluating olivine trace element thermometry

The abundance of Group II elements in olivine is dependent on closure temperature due to the temperature-dependent exchange coefficient of these elements between peridotite minerals (e.g., De Hoog et al. 2010). This allows the application of olivine geothermometers for evaluating the thermal history of peridotites. Previous studies of the thermal history of exhumed peridotites have mainly focused on pyroxene-based thermometers (Dygert and Liang 2015; Dygert et al. 2017; Grambling et al. 2022; Secchiari et al. 2022). These confirmed that for peridotites exhumed slowly to the Earth's surface, fast-diffusing species record lower temperatures compared to slow-diffusing species. Modeling of this temperature difference as a function of cooling rate, grain size, diffusivity, and initial temperature, following the formulation by Dodson (1973) and Ganguly and Tirone (1999) and the theoretical generalization for bi-mineralogic systems (Yao and Liang 2015; Liang 2015), has demonstrated that these temperatures converge at high cooling rates (Dygert and Liang 2015). These studies were limited to cpx-bearing peridotites, whereas olivine-based thermometers can be applied to clinopyroxene-poor lithologies. In addition, pyroxene-based thermometers rarely record temperatures  $< 800$  °C for abyssal peridotites due to the relatively slow diffusivities of the associated exchange systems (Fig. 8). Here, we demonstrate that olivine-based thermometers can reveal the thermal history of abyssal peridotites in the temperature range of  $\sim 650$ – $1000$  °C.

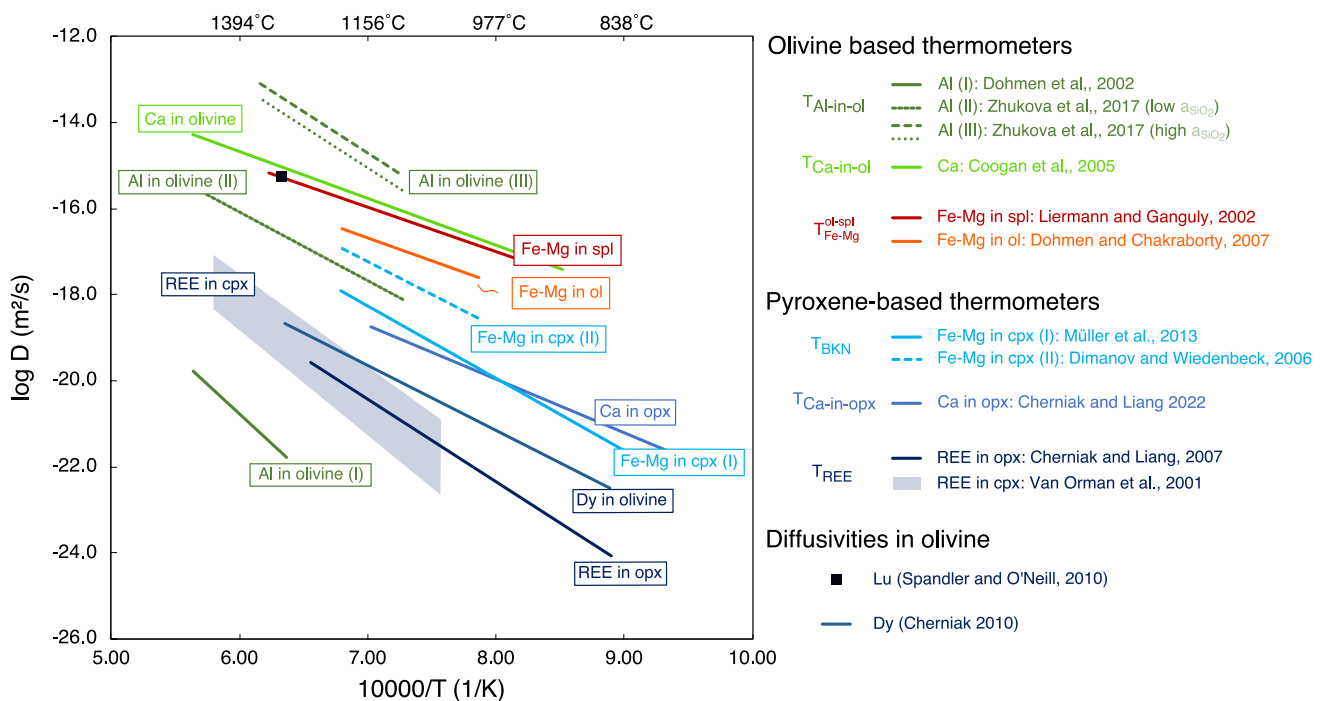


**Fig. 8** Compilation of experimentally determined Arrhenius relationships for diffusion rates of elements used for peridotite thermometry. Those that contain partial oxygen pressure ( $pO_2$ ) terms were calculated at  $pO_2 = 10^{-6.15}$  bars

We focus on application of the experimentally calibrated Al-in-olivine and Ca-in-olivine thermometers in comparison with pyroxene-based thermometers (Table 2). The Al-in-olivine thermometer ( $T_{Al}^{ol-spl}$ ; Wan et al. 2008; Coogan et al. 2014; D'Souza et al. 2020) is based on the temperature-sensitive, but pressure-independent, partitioning of Al between olivine and spinel and can be applied to all our samples (Wan et al. 2008; Coogan et al. 2014; D'Souza et al. 2020). The Ca-in-olivine thermometer ( $T_{Ca}^{ol-cpx}$ ; Shejwalkar and Coogan 2013) is based on Ca exchange between olivine and cpx, and can only be applied to the subset of our samples that contain cpx. We compare these thermometers to two commonly used thermometers for pyroxene-bearing ultramafic rocks: (1) the two-pyroxene rare earth element (REE) thermometer ( $T_{REE}$ ; Liang et al. 2013) and (2) the two-pyroxene major element thermometer ( $T_{BKN}$ ; Brey and Köhler 1990). We also evaluate the Ca-in-opx solvus thermometer ( $T_{Ca-in-opx}$ ; Brey and Köhler 1990) and the olivine-spinel Fe–Mg thermometer  $T_{Fe-Mg}^{ol-spl}$  (Li et al. 1995).

For residual abyssal peridotites (Fig. 9), pyroxene-based thermometers record higher temperatures than olivine-based thermometers, with  $T_{REE}$  being the highest (1100–1400 °C), followed by  $T_{Ca-in-opx}$  (900–1300 °C) and then  $T_{BKN}$  (800–1200 °C). The olivine-based thermometers, in contrast, record relatively lower temperatures, of which  $T_{Fe-Mg}^{ol-spl}$  is the highest (800–1000 °C), then  $T_{Ca}^{ol-cpx}$

(750–1000 °C), and finally  $T_{Al}^{ol-spl}$  recording the lowest temperatures (650–1000 °C). Literature data for xenoliths are plotted for comparison in Fig. 9. These xenoliths yield consistent temperatures among all the thermometers and plot close to the 1:1 line, except for more scatter associated with  $T_{Fe-Mg}^{ol-spl}$ . The similar temperatures recorded in these xenoliths by most thermometers is best explained by rapid emplacement and cooling (Dygert and Liang 2015).

The range of temperatures recorded in abyssal peridotites (Fig. 9) is explained by different species recording different closure temperatures (i.e., the temperature at which these species cease significant diffusive exchange with surrounding minerals; Dodson 1973; Liang 2015). During the slow cooling experienced by these peridotites, fast-diffusing species continue diffusing and equilibrating to lower temperatures. Some of the temperatures recorded by  $T_{Ca}^{ol-cpx}$  and  $T_{Al}^{ol-spl}$  are below the temperature range (950–1450 °C) of their original experimental calibration (Wan et al. 2008; Shejwalkar and Coogan 2013; D'Souza et al. 2020) and thus have higher uncertainties. The thermometric equations applied here are fitted against thermodynamic formulations, which allows for extrapolation beyond the range of the experimental calibrations. Relative differences in temperatures that we obtained between peridotites from different settings should thus remain meaningful despite the higher uncertainties associated with their absolute values.

**Table 2** Summary of  $T_{\text{Al}}^{\text{ol-spl}}$ ,  $T_{\text{BKN}}$ ,  $T_{\text{Ca}}^{\text{ol-cpx}}$ ,  $T_{\text{Ca-in-opx}}$ ,  $T_{\text{Fe-Mg}}^{\text{ol-spl}}$  and  $T_{\text{REE}}$  values in °C

| Sample ID                          | Lithology                        | Ridge  | $T_{\text{Al}}^{\text{ol-spl}}$ | $1\sigma$ | $T_{\text{BKN}}$ | $T_{\text{Ca}}^{\text{ol-cpx}}$ | $1\sigma$ | $T_{\text{Ca-in-opx}}$ | $T_{\text{Fe-Mg}}^{\text{ol-spl}}$ | $T_{\text{REE}}$ | $1\sigma$ |
|------------------------------------|----------------------------------|--------|---------------------------------|-----------|------------------|---------------------------------|-----------|------------------------|------------------------------------|------------------|-----------|
| <i>Residual peridotites</i>        |                                  |        |                                 |           |                  |                                 |           |                        |                                    |                  |           |
| HLY0102-70-87                      | Lherz                            | Gakkel | 767                             | 76        | n.d.             | 888                             | 62        | 1267                   | 980                                | n.d.             | n.d.      |
| HLY0102-87-37                      | Harz                             | Gakkel | 943                             | 20        | n.d.             | 960                             | 32        | 1188                   | 901                                | n.d.             | n.d.      |
| PS59-235-1                         | Lherz                            | Gakkel | 920                             | 53        | 1182             | 966                             | 51        | 1274                   | 820                                | 1054             | 27        |
| PS59-235-17                        | Lherz                            | Gakkel | 900                             | 47        | 1033             | 939                             | 39        | 1203                   | 835                                | 1153             | 15        |
| PS59-235-18                        | Lherz                            | Gakkel | 929                             | 32        | 1317             | 983                             | 22        | 1472                   | 871                                | n.a.             | n.a.      |
| PS59-249-12                        | Harz                             | Gakkel | 760                             | 37        | n.d.             | 880                             | 53        | 1077                   | 964                                | n.d.             | n.d.      |
| PS59-249-60                        | Harz                             | Gakkel | 755                             | 26        | n.d.             | 906                             | 36        | 961                    | 851                                | n.d.             | n.d.      |
| PS59-249-74                        | Harz                             | Gakkel | 797                             | 51        | n.d.             | 904                             | 32        | 1151                   | 855                                | n.d.             | n.d.      |
| Kn162-9-37-10                      | Harz                             | SWIR   | 726                             | 32        | 872              | 825                             | 21        | 1027                   | 934                                | 1340             | 36        |
| Kn162-9-37-14                      | Harz                             | SWIR   | 756                             | 31        | n.d.             | 877                             | 24        | 1245                   | 927                                | n.d.             | n.d.      |
| Kn162-9-50-7                       | Lherz                            | SWIR   | 892                             | 18        | 1066             | 936                             | 39        | 1257                   | 914                                | 1254             | 14        |
| Kn162-9-55-23                      | Lherz                            | SWIR   | 781                             | 31        | 992              | 887                             | 28        | 1363                   | 922                                | 1028             | 59        |
| Kn162-9-58-16                      | Harz                             | SWIR   | 755                             | 29        | 1193             | 848                             | 23        | 1231                   | 917                                | n.d.             | n.d.      |
| Kn162-9-59-2                       | Lherz                            | SWIR   | 840                             | 65        | 913              | 909                             | 41        | 1306                   | 981                                | 1237             | 33        |
| Kn162-9-59-7                       | Lherz                            | SWIR   | 763                             | 45        | 989              | 898                             | 24        | 1257                   | 930                                | 1330             | 21        |
| PS86-6-26                          | Lherz                            | SWIR   | 764                             | 51        | 1094             | 818                             | 65        | 1186                   | 854                                | 1381             | 81        |
| Van7-85-27                         | Harz                             | SWIR   | 858                             | 56        | 1095             | 902                             | 8         | 1228                   | 837                                | 1314             | 74        |
| Van7-85-30                         | Harz                             | SWIR   | 751                             | 32        | 1056             | 894                             | 17        | 1181                   | 783                                | 1311             | 146       |
| Van7-85-47                         | Lherz                            | SWIR   | 804                             | 28        | 1130             | 909                             | 37        | 1349                   | 882                                | 1177             | 34        |
| Van7-85-49                         | Lherz                            | SWIR   | 866                             | 34        | 1157             | 913                             | 38        | 1211                   | 846                                | 1336             | 53        |
| 895A 2R-1, 7–10 cm                 | Harz                             | EPR    | 922                             | 38        | n.d.             | 971                             | 41        | 1299                   | 915                                | n.d.             | n.d.      |
| 895D 2R-2, 43–46 cm                | Harz                             | EPR    | 990                             | 48        | n.d.             | 1024                            | 60        | 1247                   | 918                                | n.d.             | n.d.      |
| 895D 4R-3, 56–60 cm                | Harz                             | EPR    | 1026                            | 54        | n.d.             | 998                             | 57        | 1315                   | 933                                | n.d.             | n.d.      |
| 895D 5R-1, 7–11 cm                 | Harz                             | EPR    | 997                             | 42        | n.d.             | 1014                            | 53        | 1290                   | 956                                | n.d.             | n.d.      |
| BMRG08-98-1-12                     | Harz                             | Tonga  | 785                             | 37        | 1357             | 850                             | 41        | 1192                   | 863                                | n.a.             | n.a.      |
| BMRG08-98-2-7                      | Harz                             | Tonga  | 766                             | 63        | 1018             | 825                             | 50        | 1171                   | 905                                | 1271             | 10        |
| BMRG08-98-2-8                      | Harz                             | Tonga  | 770                             | 53        | 1094             | 826                             | 44        | 1146                   | 905                                | 1423             | 60        |
| BMRG08-98-2-18                     | Harz                             | Tonga  | 757                             | 51        | 1096             | 856                             | 55        | 1134                   | 884                                | 1356             | 77        |
| BMRG08-98-2-23                     | Harz                             | Tonga  | 766                             | 57        | 1041             | 884                             | 37        | 1130                   | 924                                | 1278             | 21        |
| BMRG08-98-2-25                     | Harz                             | Tonga  | 761                             | 53        | 963              | 859                             | 49        | 1224                   | 903                                | 1146             | 5         |
| <i>Melt-influenced peridotites</i> |                                  |        |                                 |           |                  |                                 |           |                        |                                    |                  |           |
| HLY0102-04-63                      | Plag lherz                       | Gakkel | 868                             | 30        | 1129             | 920                             | 29        | 1123                   | 899                                | 1420             | 30        |
| Kn162-9-58-30                      | Plag lherz                       | SWIR   | 772                             | 35        | 964              | 852                             | 18        | 1213                   | 912                                | 1215             | 15        |
| PS86-6-39                          | Lherz                            | SWIR   | 794                             | 24        | 1009             | 894                             | 16        | 1103                   | 852                                | 1113             | 3         |
| Van7-78-40                         | Plag harz                        | SWIR   | 881                             | 77        | 931              | 845                             | 33        | 1220                   | 781                                | 875              | 111       |
| Van7-96-28                         | Plag lherz                       | SWIR   | 763                             | 14        | 1115             | 828                             | 48        | 1337                   | 818                                | 1113             | 39        |
| BMRG08-106-1-2                     | Harz                             | Tonga  | 711                             | 25        | 773              | 783                             | 58        | 903                    | 821                                | 1172             | 57        |
| BMRG08-106-1-5                     | Harz                             | Tonga  | 685                             | 46        | 807              | 768                             | 41        | 864                    | 844                                | 1112             | 14        |
| BMRG08-106-1-15                    | Dunite                           | Tonga  | 673                             | 66        | n.d.             | n.d.                            | n.d.      | n.d.                   | 803                                | n.d.             | n.d.      |
| BMRG08-106-1-17                    | Harz                             | Tonga  | 658                             | 24        | 762              | 730                             | 30        | 1018                   | 867                                | 677              | 3         |
| <i>Melt-veined peridotites</i>     |                                  |        |                                 |           |                  |                                 |           |                        |                                    |                  |           |
| PS59-235-04                        | Ol websterite                    | Gakkel | 899                             | 36        | 1288             | 918                             | 42        | 1259                   | 1063                               | n.a.             | n.a.      |
| Van7-78-25                         | Dunite w/gabbro vein             | SWIR   | 843                             | 28        | n.d.             | 878                             | 50        | n.d.                   | 743                                | n.d.             | n.d.      |
| Van7-78-31M                        | Plag peridotite w/gabbro vein    | SWIR   | 824                             | 26        | 871              | 810                             | 26        | 1168                   | 763                                | 1096             | 4         |
| Van7-78-36A                        | Plag peridotite matrix           | SWIR   | 783                             | 20        | 744              | 797                             | 17        | 950                    | 788                                | 1167             | 34        |
| Van7-78-36B                        | Plag peridotite with gabbro vein | SWIR   | 814                             | 78        | 744              | 851                             | 28        | 950                    | 826                                | 1317             | 0         |

$P = 15$  kbar is assumed for  $T_{\text{Ca}}^{\text{ol-cpx}}$ ,  $T_{\text{Ca-in-opx}}$ , and  $T_{\text{BKN}}$

n.a. = not applicable, indicates that REEs from the two pyroxenes are out of equilibrium and, therefore, excluded

n.d. = no data, corresponding to samples for which analyzable cpx is not present and thus  $T_{\text{BKN}}$  and  $T_{\text{REE}}$  cannot be calculated

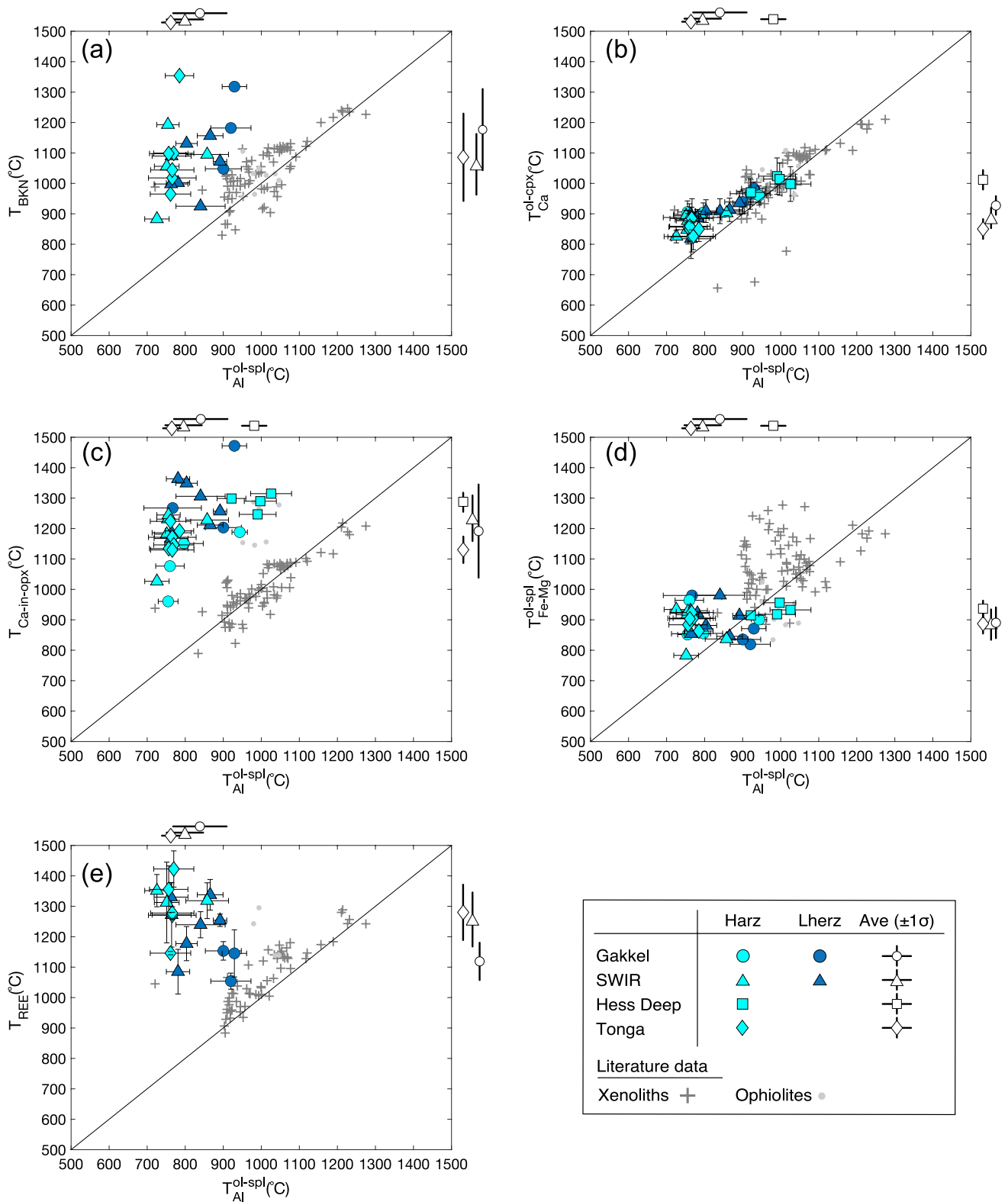


**Fig. 9** Variation of temperatures estimated using  $T_{Al-Cr}^{ol-spl}$  and **a**  $T_{BKN}$ , **b**  $T_{Ca}^{ol-cpx}$ , **c**  $T_{Ca-in-opx}$ , **d**  $T_{Fe-Mg}^{ol-spl}$ , and **e**  $T_{REE}$ . Data are shown relative to the 1:1 correspondence line. Abyssal peridotites plot away from this line, indicating different closure temperatures due to their slow

emplacement on the seafloor. For comparison, xenoliths are rapidly emplaced and record similar temperatures with all thermometers (xenolith data from Witt-Eickischen and O'Neill 2005; Witt-Eickischen et al. 2009; Mallmann et al. 2009; De Hoog et al. 2010; Quinn et al. 2018; Canil et al. 2021; Canil and Russell 2022)

The order of temperatures recorded by different thermometers in a single abyssal peridotite sample matches the order of diffusivities for the components used in the thermometers (Fig. 8). The REEs in pyroxenes diffuse the slowest (Van Orman et al. 2001; Cherniak and Liang 2007), followed by Ca in opx (Cherniak and Liang 2022), Fe–Mg in cpx (Dimanov and Wiedenbeck 2006; Müller et al. 2013), Fe–Mg in spinel and olivine (Dohmen and Chakraborty 2007), and finally Ca in olivine (Coogan et al. 2005). Multiple substitutional mechanisms have been proposed for Al in olivine, with associated diffusivities ranging from extremely slow (substituting Si into the olivine tetrahedral site; Dohmen 2002) to a rapid subsidiary mechanism dependent on Si activity (Zhukova et al. 2017). Our temperature estimates from  $T_{\text{Al}}^{\text{ol}-\text{spl}}$  are even lower than  $T_{\text{Ca}}^{\text{ol}-\text{cpx}}$ , which suggests that Al diffuses faster than Ca in olivine and favors the diffusivity determined by Zhukova et al. (2017). As spinel Cr# is affected by subsolidus cooling (Voigt and von der Handt 2011), which may affect the calculated  $T_{\text{Al}}^{\text{ol}-\text{spl}}$ , we ran a model to demonstrate that the effect of spinel Cr# redistribution with temperature is minimal (Supplementary Material E). Instead, the variation of  $T_{\text{Al}}^{\text{ol}-\text{spl}}$  is mostly controlled by Al in olivine (Fig. S5). Overall, the temperatures in a single peridotite from high to low match the exact order from slow to fast for the diffusivity data upon which the thermometer depends (Figs. 8, 9). This supports previous interpretations that thermometers based on faster diffusing species will record lower temperatures, particularly when cooling is sufficiently slow (Ozawa 1983; Liang et al. 2013; Dygert and Liang 2015).

Temperature estimates by olivine-based thermometers show differences between the tectonic environments, in contrast with the similar temperature ranges recorded by pyroxene-based thermometers across all tectonic settings (Fig. 9). To illustrate this, average and one-standard deviation temperatures were calculated for each tectonic setting (Fig. 9). The Hess Deep harzburgites from the fast-spreading EPR have higher  $T_{\text{Al}}^{\text{ol}-\text{spl}}$  and  $T_{\text{Ca}}^{\text{ol}-\text{cpx}}$  values than peridotites from the ultraslow-spreading SWIR and Gakkel (Fig. 9b). Hess Deep harzburgites also have elevated abundances of other Group II elements (Cr and V; Fig. 5c, d), suggesting similar, temperature-sensitive partitioning behavior. The olivine-based temperature differences between tectonic settings are also consistent with the subsolidus cooling model for Group III elements in olivine that we present in the “**Partial melting and sub-solidus redistribution: Ti, Y, and Yb**” section.

Variations in closure temperature as a function of spreading rate can be caused by contrasting cooling rates and/or initial temperatures (Ganguly and Tirone 1999; Dygert and Liang 2015). We attribute the differences in  $T_{\text{Al}}^{\text{ol}-\text{spl}}$  and

$T_{\text{Ca}}^{\text{ol}-\text{cpx}}$  among the ridge peridotites to contrasting cooling rates for two reasons. First, the pyroxene-based thermometers from Gakkel and SWIR also record high temperatures > 1000 °C, suggesting that initial temperatures were similar across tectonic settings. Second, predictions of mantle potential temperature based on geophysical constraints indicate no temperature differences in these regions (Dalton et al. 2014).

The contrast in cooling rate between the ridges agrees with their geological settings. Harzburgites from Hess Deep experienced faster cooling as uplift and emplacement is faster at faster spreading rates (e.g., Coogan et al. 2007). In contrast, peridotites from ultraslow spreading ridges are exhumed more slowly, experiencing a longer period of conductive cooling (Cannat 1996; Sauter et al. 2013; Liu et al. 2020). Besides tectonic emplacement, hydrothermal circulation can also affect cooling rates and the observed closure temperatures. Although hydrothermal circulation is typically associated with temperatures < 600 °C, multiple studies at Hess Deep have suggested that seawater influx to lower crustal and upper mantle depths likely reached temperatures of 600–750 °C (Manning and MacLeod 1996; Manning et al. 2000; Grambling et al. 2022). Since peridotites from the same locality likely have experienced similar exhumation mechanisms, the scatter among them might be caused by variations in the extent of hydrothermal circulation, leading to uneven cooling rates.

Compared to temperature averages for ridge peridotites, average peridotite from the Tonga forearc have similar  $T_{\text{REE}}$ ,  $T_{\text{BKN}}$ , and  $T_{\text{Ca-in-opx}}$ , and slightly lower average  $T_{\text{Al}}^{\text{ol}-\text{spl}}$  and  $T_{\text{Ca}}^{\text{ol}-\text{cpx}}$  (Fig. 9b). The melt-influenced Tonga peridotites record the lowest average temperatures in our peridotite data set (Fig. 10). These observations suggest that the Tonga peridotites have similar cooling histories to the ridge peridotites at temperatures > 1000 °C, but then experienced slow cooling between ~ 600–1000 °C that overlaps with peridotites from ultraslow spreading ridges. Birner et al. (2017) concluded that the petrogenesis of the Tonga residual peridotites is best explained by high degrees of melting during subduction initiation. At this stage, the mantle wedge experiences adiabatic decompression melting due to near-trench spreading, which tectonically resembles mid-ocean ridge melting and produces forearc basalts that are compositionally similar to MORB (Reagan et al. 2010; Stern and Gerya 2018). This geodynamic resemblance can account for the similar temperatures recorded by Tonga and ridge peridotites at higher temperatures following melting (i.e.,  $T_{\text{REE}}$ ,  $T_{\text{BKN}}$  and  $T_{\text{Ca-in-opx}}$  at  $T > 1000$  °C). These Tonga peridotites are later exhumed at the trench inner wall due to tectonic erosion (Clift 1998; Birner et al. 2017), which is a different exhumation mechanism that lacks mantle upwelling compared to

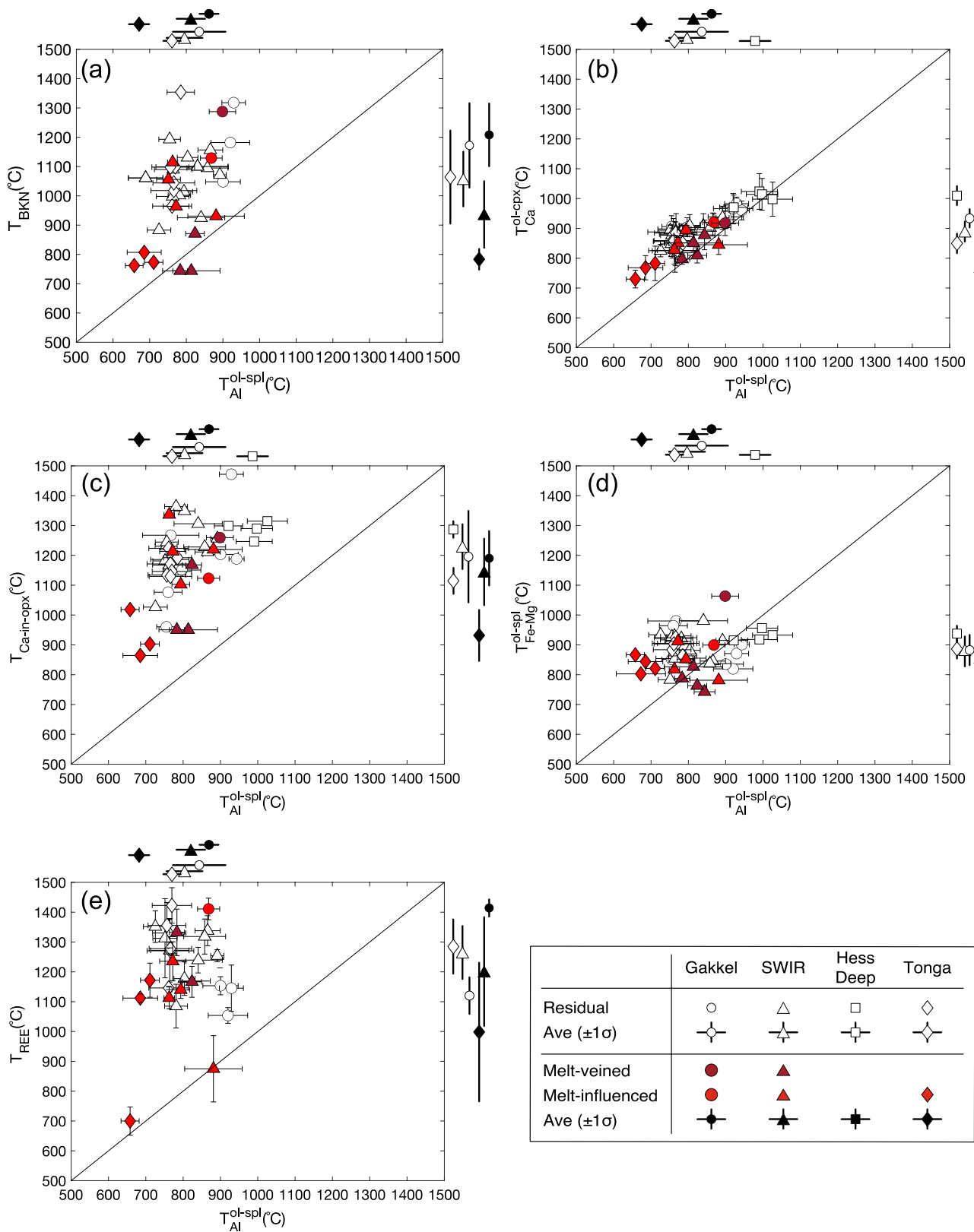


**Fig. 10** Same as Fig. 9, but with melt-influenced (red symbols) and melt-veined (maroon symbols) peridotites included. Residual peridotites are plotted as open symbols to highlight the contrast between these and melt-influenced and melt-veined peridotites

ridge peridotites. The overall outcome appears to be a relatively slow exhumation rate, comparable to ultraslow spreading ridges, which accounts for the similar  $T_{\text{Al}}^{\text{ol-spl}}$  and  $T_{\text{Ca}}^{\text{ol-cpx}}$  recorded at 650–1000 °C.

Although the melt-influenced and melt-veined data set presented here is small, we observe differences in their closure temperatures when compared to residual peridotites (Fig. 10). For thermometers utilizing relatively fast-diffusing species ( $T_{\text{BKN}}$ ,  $T_{\text{Al}}^{\text{ol-spl}}$ ,  $T_{\text{Ca}}^{\text{ol-cpx}}$ , and  $T_{\text{Fe-Mg}}^{\text{ol-spl}}$ ), the melt-veined peridotites from SWIR show a better agreement among the thermometers and plot close to the 1:1 line (Fig. 10a, b, d). We interpret these temperatures as the final equilibration temperatures after gabbroic melt (> 1100 °C) intrudes into relatively cold peridotite in slowly ascending mantle. The presence of melt may thermally facilitate diffusive exchange between minerals and thus promote re-equilibration, resulting in close agreement among  $T_{\text{BKN}}$ ,  $T_{\text{Al}}^{\text{ol-spl}}$ ,  $T_{\text{Ca}}^{\text{ol-cpx}}$ , and  $T_{\text{Fe-Mg}}^{\text{ol-spl}}$  (Fig. 10). These thermometers in our SWIR melt-veined data set record temperatures of ~800 °C, which we interpret as the final temperature of equilibration following melt addition. The melt-veined peridotite from Gakkel records similar  $T_{\text{Al-Cr}}^{\text{ol-spl}}$  and  $T_{\text{Ca}}^{\text{ol-cpx}}$  (Fig. 10b), but not  $T_{\text{BKN}}$  and  $T_{\text{Fe-Mg}}^{\text{ol-spl}}$  (Fig. 10a, d, respectively). This might be due to the rock being an olivine websterite, which is lithologically distinct from the SWIR gabbro-veined peridotites, but is also difficult to interpret given that only one sample is available.

When melt-influenced and melt-veined peridotites are compared to residual peridotites based on tectonic settings, peridotites from Tonga preserve the most significant difference (Fig. 10). For all six thermometers, the melt-influenced peridotites from Tonga record lower average temperatures than the residual peridotites. Apart from recording lower temperatures, these peridotites have imprints of melt in the form of enriched clinopyroxene LREEs and either interstitial clinopyroxene or enriched spinel  $\text{TiO}_2$  (Figs. 2, 3). One possibility is that trace amounts of melt infiltrated the system during cooling, which may have thermally facilitated diffusive exchange, promoting re-equilibration at lower temperatures. However, this temperature difference between melt-influenced and residual peridotites is less distinctive at SWIR. More observations are needed to investigate whether this contrasting observation between Tonga and SWIR reflects different melt compositions, different timing or style of melt–rock interaction, or different exhumation mechanisms.

To summarize, we observe differences in temperatures recorded by olivine-based thermometers, particularly  $T_{\text{Al}}^{\text{ol-spl}}$  and  $T_{\text{Ca}}^{\text{ol-cpx}}$ , as a function of tectonic setting. Over the temperature interval 600–1000 °C, Hess Deep harzburgites from the fast-spreading EPR record the highest temperatures, followed by peridotites from the ultra-slow spreading Gakkel

and SWIR, and the Tonga forearc peridotites with slightly lower average temperatures. In the next section, we demonstrate that subsolidus re-equilibration recorded by olivine Group III elements agree with this order of cooling rates. From comparison of residual peridotites to melt-influenced and melt-veined peridotites, we suggest that the presence of melt can facilitate diffusive equilibrium between peridotite minerals. Overall, our results highlight the utility of olivine-based thermometers for studying thermal histories of clinopyroxene-poor lithologies and exploring tectonic processes within the 600–1000 °C temperature interval.

### Partial melting and subsolidus redistribution: Ti, Y, and Yb

In this section, we use the systematics of Group III elements in residual peridotites to explore the extent of partial melting and subsolidus re-equilibration (Fig. 11). The extent of melting experienced by residual peridotites are conventionally estimated from the concentrations of high field strength elements and REEs in clinopyroxene (e.g., Johnson et al. 1990; Bizimis et al. 2000; Warren and Shimizu 2010; Birner et al. 2017). Because these elements are also incompatible in olivine during mantle melting, we expect their contents in olivine to similarly record the degree of partial melting. When olivine Ti is plotted against Yb and Y (Fig. 11a, b, respectively), the residual peridotites form a gradual depletion trend, from fertile (clinopyroxene-rich) lherzolites to harzburgites to clinopyroxene-poor harzburgites, which have the lowest concentrations. The decrease in clinopyroxene mode from clinopyroxene-rich lherzolites to clinopyroxene-poor harzburgites reflects an increasing degree of partial melting (e.g., Dick et al. 1984), which suggests that Group III element abundances in olivine are also controlled by partial melting. Here, we show that the relative abundances of Group III elements reflect the degree of partial melting, but that absolute concentrations have been reset by subsolidus redistribution.

### Melting model

To test whether olivine Group III elements can provide quantitative estimates of the degree of partial melting, we used a non-modal fractional melting model for olivine following previous models for melting of peridotite bulk rock (e.g., Shaw, 1970) and clinopyroxene (Johnson et al. 1990):

$$\frac{C_A^i}{C_{0,A}^i} = \left( 1 - \frac{P^i F}{D_0^i} \right)^{\frac{1}{D^i} - 1} \quad (1)$$

where  $A$  is the mineral (ol, opx, or cpx) and  $i$  is the element of interest;  $C_A^i$  is the concentration of  $i$  in mineral  $A$ ;  $C_{0,A}^i$  is

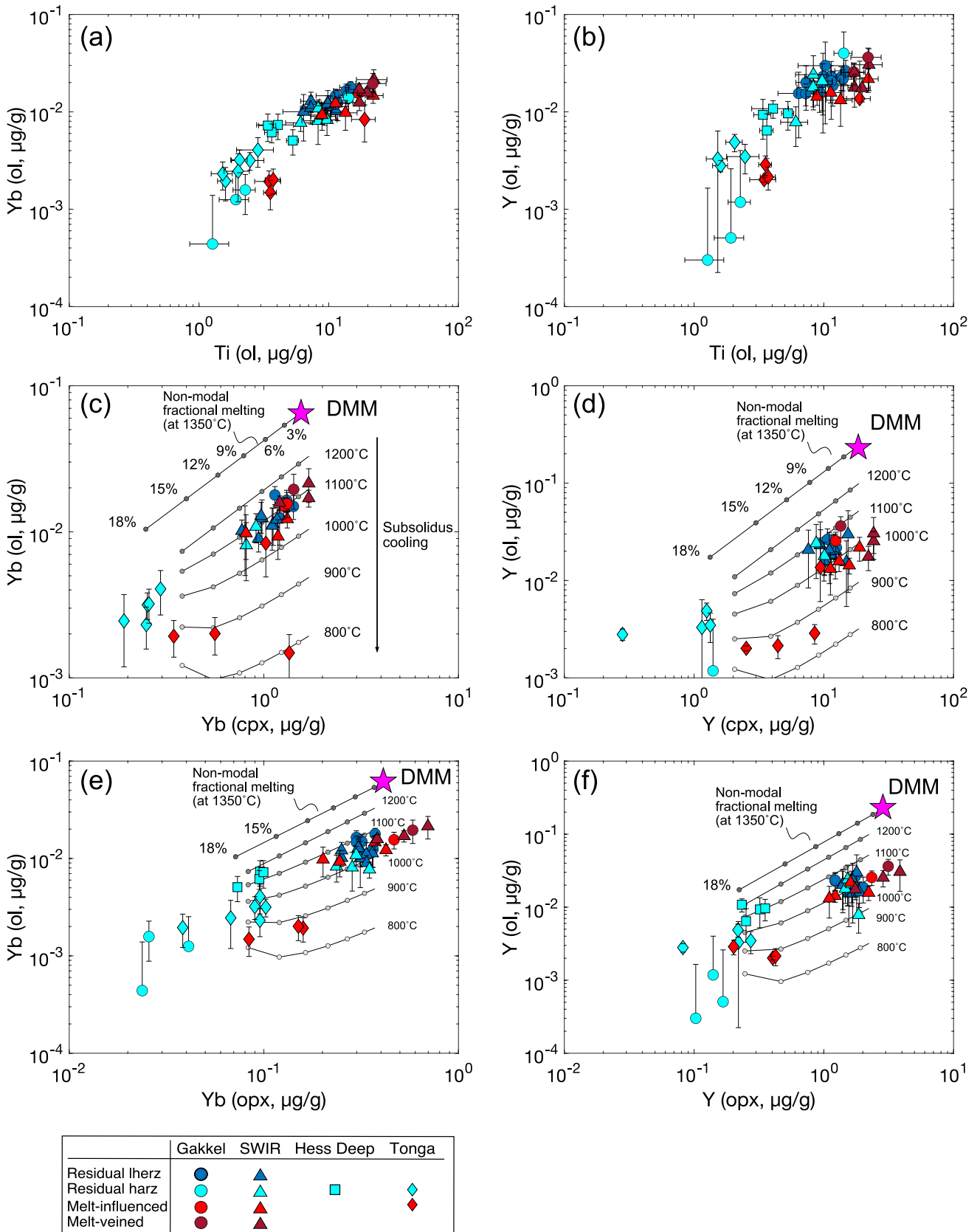


**Fig. 11** Variation in olivine of **a** Yb as a function of Ti and **b** Y as a function of Ti. Co-variation in olivine and cpx of **c** Yb and **d** Y. Co-variation in olivine and opx of **e** Yb and **f** Y opx. Lines illustrate the melting and subsolidus redistribution model isotherms from 1200 down to 800 °C (see text for details) and dots indicate increments of 3% melting

the concentration of  $i$  in mineral  $A$  before melting; and  $F$  is the degree of partial melting. The parameter  $D_0^i$  is the bulk rock/melt partition coefficient before melting, defined as

$$D_0^i = \sum D_A^i x_A \quad (2)$$

where  $D_A^i$  is the mineral  $A$ /melt partition coefficient of the element  $i$  and  $x_A$  is the starting mode of mineral  $A$ . The parameter  $P^i$  is defined as

$$P^i = \sum D_A^i p_A \quad (3)$$

where  $p_A$  is the coefficient for mineral  $A$  in the melting reaction.

For our model calculations, we used the depleted MORB mantle (DMM) model composition from Workman and Hart (2005) to define the initial elemental concentrations and mineral modes. Melting reaction coefficients for fertile lherzolite were used from Wasylenko (2003), and partition coefficients were calculated at 1350 °C from the experimentally parameterized lattice strain models compiled in Sun and Liang (2014) (summarized in Table S10 in Supplementary Material F). Detailed evaluation of parameters in this melting model can be found in Warren (2016). We used this model to calculate the trace element content in olivine and clinopyroxene in a residual peridotite for melting up to  $F=18\%$ . As shown in Fig. 11c, the model predicts higher Yb concentrations in olivine than observed for a given clinopyroxene Yb content. Since this model can readily reproduce the Yb and Y contents for both pyroxenes at various degrees of melting (Fig. S6a, b), the misfit in Fig. 11c is likely due to the model overestimating olivine Yb contents. This overestimation is also observed for Y in olivine (Fig. 11d).

Experimentally parameterized lattice strain models predict that olivine experiences diffusive loss of Group III elements to coexisting clinopyroxene during cooling. Collectively, the lattice strain models for REEs and Y in olivine (Sun and Liang 2013a), orthopyroxene (Yao et al. 2012; Sun and Liang 2013b), and clinopyroxene (Sun and Liang 2012) predict increases of  $D_{cpx/ol}^i$ ,  $D_{opx/ol}^i$ , and  $D_{cpx/opx}^i$  as temperature decreases (Sun and Liang 2014, where  $i$  denotes Yb or Y). These increases imply that during cooling, clinopyroxene gains REEs from coexisting olivine and orthopyroxene, while olivine loses REEs to pyroxenes.

To evaluate the redistribution of Yb and Y in olivine after melting, we calculated the mineral–mineral partition

coefficients at 1350 °C using the models above (see Table S10 in the Supplementary Material F for parameters). In Fig. S7, these are compared with the observed mineral–mineral partition coefficients, which are calculated from the measured concentrations in our minerals. For  $D_{cpx/opx}^i$ , the predicted and observed partition coefficients cluster around the 1:1 line (Fig. S7a, b). This agreement between cpx and opx suggests that the pyroxene Yb and Y distribution in abyssal peridotites have not been significantly modified by subsolidus redistribution, in agreement with the high closure temperatures for these elements in pyroxenes (Liang et al. 2013; Dygert and Liang 2015). In contrast, most of the observed  $D_{cpx/ol}^{Yb}$  and  $D_{cpx/ol}^Y$  values are higher than the predicted values, implying that olivine lost Yb and Y during subsolidus cooling. This agrees with previous observations and model predictions of subsolidus cooling effects in peridotites (Sun and Liang 2014; Liang et al. 2021).

Subsolidus redistribution of Group III elements between olivine and pyroxenes has a much greater effect on element abundances in olivine than in pyroxenes, because olivine contains much lower abundances of these elements (olivine = 0.7–5 ng/g; orthopyroxene = 38–400 ng/g; clinopyroxene = 70–1880 ng/g for Yb in this study). In a hypothetical system of 100 g peridotite with 70% olivine, 20% orthopyroxene and 10% clinopyroxene that has 10, 200, and 1000 ng/g Yb, respectively, a 5 ng/g reduction in olivine Yb content would increase orthopyroxene Yb by 17 ng/g or clinopyroxene Yb by 35 ng/g. Both these increases are negligible when compared to their original Yb concentrations.

### Subsolidus redistribution model

To quantify the effects of subsolidus redistribution on olivine Group III elements, we constructed a temperature-dependent, closed-system subsolidus re-equilibration model based on the formulation by Liang et al. (2021). We implemented this model as a follow-on stage to our non-modal fractional melting model. For simplicity, we assumed closed-system conditions and that chemical equilibrium is maintained at various stages of cooling. According to mass balance:

$$C_s^i = w_{cpx} C_{cpx}^i + w_{opx} C_{opx}^i + w_{ol} C_{ol}^i + w_{spl} C_{spl}^i \quad (4)$$

where  $C_s^i$  is the bulk rock composition of element  $i$ ,  $w$  is the modal proportion of the corresponding mineral, and  $C_A^i$  is the concentration of  $i$  in mineral  $A$ . We dropped the spinel term in Eq. 4, since spinel hosts very small amounts of the elements of interest here. Equation 4 can be re-arranged with respect to  $C_{ol}^i$ :

$$C_{ol}^i = \frac{C_s^i}{w_{cpx} \frac{C_{cpx}^i}{C_{ol}^i} + w_{opx} \frac{C_{opx}^i}{C_{ol}^i} + w_{ol}} \quad (5)$$

Assuming equilibrium, then  $C_{cpx}^i/C_{ol}^i$  and  $C_{opx}^i/C_{ol}^i$  are equivalent to  $D_{cpx/ol}^i$  and  $D_{opx/ol}^i$ , respectively, which yields:

$$C_{ol}^i = \frac{C_s^i}{w_{cpx} D_{cpx/ol}^i + w_{opx} D_{opx/ol}^i + w_{ol}} \quad (6)$$

At a given temperature, the  $D^i$  values were obtained from the lattice strain models (Sun and Liang 2014). Further details of the model are discussed in the Supplementary Material F. Because a temperature-dependent lattice strain model is not available for  $D_{ol/melt}^{Ti}$ , we only modeled Yb and Y. Due to the co-variation of Ti with both Yb and Y (Fig. 11a, b), we expect the behavior of Ti in olivine to be similar during melting and subsolidus cooling.

Our two-stage model simulates the scenario where a peridotite experienced melting and then underwent subsolidus cooling during uplift and emplacement on the seafloor. Trace elements in olivine continue to re-equilibrate with adjacent pyroxenes until the closure temperature for diffusive exchange is reached. The output of the partial melting model ( $C_s^i$ ; Eq. 1) is thus used as the starting concentration in Eq. 6, which allows the re-equilibrated concentration at a lower temperature ( $C_{ol}^i$ ) to be calculated. We used our two-stage model to investigate the temperature range 800–1200 °C (Fig. 11c–f). As temperature decreases, the model isotherms increasingly show concave-upward geometries, with large concavities at high extents of melting. We interpret the concavity to be the outcome of the modal mineralogy effect outweighing other factors in the model: at high degrees of melting ( $F \sim 18\%$ ), the modal cpx content is so low that very little Yb and Y are re-distributed to maintain equilibrium and mass balance in a closed system.

Overall, our model illustrates that lower equilibrium temperatures result in lower olivine trace element abundances at similar pyroxene trace element abundances. Our model isotherms (Fig. 11) fit the observed concentrations of Yb and Y in olivine, clinopyroxene, and orthopyroxene for subsolidus re-equilibration over a temperature range of 800–1000 °C. In contrast, trace elements in clinopyroxene and orthopyroxene remain at near-solidus (1350 °C) abundances (Fig. S6a, b). This confirms that diffusion of trace elements between clinopyroxene and orthopyroxene terminated at higher, near solidus temperatures (Liang et al. 2013), whereas trace elements continued to diffuse out of olivine until lower temperatures ( $\sim 800$  °C).

## Two-stage model results by tectonic setting

The two-stage model reproduces the contrasting closure temperatures observed among our abyssal peridotite localities. This reflects the control on peridotite thermal histories at different tectonic regimes by their different cooling rates and agrees with our inferences from thermometry results in the “Evaluating olivine trace element thermometry” section. The olivine Yb and Y contents of residual peridotites from Gakkel and SWIR place them between the 1000 and 1100 °C model isotherms for the subsolidus re-equilibration model (Fig. 11c–f), suggesting that these elements in olivine re-equilibrated until slightly above 1000 °C. The only exceptions are three strongly depleted, clinopyroxene-poor Gakkel harzburgites, all of which have experienced high extents of melting and have Yb and Y contents below our model predictions. The Hess Deep harzburgites, in contrast, plot at temperatures of 1100–1200 °C (Fig. 11e, f), which agrees with the faster exhumation predicted for Hess Deep based on its faster spreading rate.

Compared to most ridge peridotites, peridotites from Tonga record lower closure temperatures and fall between the modeled 900–1000 °C isotherms, indicating relatively slower cooling rates that agree with their lower  $T_{Al-Cr}^{ol-spl}$  and  $T_{Ca}^{ol-cpx}$  (“Evaluating olivine trace element thermometry” section, Fig. 9b). We emphasize that these Tonga harzburgites have other geochemical characteristics identical to the Hess Deep harzburgites (e.g., high spinel Cr#, low clinopyroxene modal abundance, low pyroxene Yb and Y contents), but their olivine trace element contents are very different (Figs. 5, 11). These observations suggest that while both Tonga and Hess Deep harzburgites underwent very high degrees of melting (Dick and Natland 1996; Birner et al. 2017), olivine trace elements show the exhumation rate at Tonga was slower than in ridge environments.

## Melt-influenced and melt-veined peridotites

The melt-veined peridotites from Gakkel and SWIR have Yb and Y in olivine, orthopyroxene, and clinopyroxene higher than most residual peridotites (Fig. 11) and roughly fall along the same modeled 1000–1100 °C isotherms with the Gakkel and SWIR residual peridotites. We interpret this as enrichment caused by melt-infiltration. In contrast, melt-influenced peridotites from Gakkel and SWIR mostly overlap with their residual counterparts, indicating that melt–rock interaction at low melt–rock ratios has little effect on the Yb and Y in mantle minerals (Fig. 11).

At Tonga, the melt-influenced peridotites have higher Yb and Y in pyroxenes compared to the residual peridotites (Figs. 2, 11). However, they have lower Yb and Y in olivine, plotting between the 800 and 900 °C model isotherms (Fig. 11c–f). This record of lower closure temperature agrees with our thermometry results (“[Evaluating olivine trace element thermometry](#)” section; Fig. 10). A possible explanation is that the presence of melt during cooling can thermally facilitate diffusive exchange and equilibration to lower temperatures. While this might be the case at Tonga, melt-influenced peridotites and residual peridotites from other settings share similar olivine Yb and Y contents, leaving the processes behind this observation to be further investigated.

To summarize, the Yb and Y abundances in abyssal peridotite olivine form a depletion trend that reflects the extent of melt depletion, yet the absolute values do not match predictions for the residues of melting. Our two-stage model, consisting of mantle melting followed by subsolidus re-equilibration, reproduces the co-variation in Group III element abundances between pyroxenes and olivine. This suggests that olivine has diffusively lost these elements during subsolidus cooling. The re-equilibration temperatures recorded by Yb and Y in olivine vary among the peridotites with tectonic settings with Hess Deep having the highest, followed by Gakkel and SWIR, and Tonga having the lowest temperatures. This reflects the contrasting cooling rates among these different tectonic environments and agrees with our geothermometry observations in “[Evaluating olivine trace element thermometry](#)” section.

## Conclusions

In this study, we analyzed trace elements in olivine from abyssal peridotites to investigate their behavior during formation and evolution of the lithosphere at ridges and subduction zones. We categorized our peridotites into residual, melt-influenced, and melt-veined peridotites based on petrographic and geochemical characteristics and compared each category. We found that the systematics of olivine trace elements in abyssal peridotites follow the De Hoog et al. (2010) classification into Group I–III elements. Analyses of each of these groups reveals aspects of olivine geochemistry that can be used to understand the petrogenesis of the oceanic lithosphere:

- Group I elements, including Ni, Zn, Co, and Mn, are dominantly hosted in olivine in peridotites. We found that melt-veined peridotites have higher Mn, Co, Zn and lower Ni, Fo, and Ni/Co contents compared to residual peridotites. This highlights their potential as tracers of melt–rock interaction.
- Group II elements are Al, Ca, Cr, and V. Their abundances in olivine are strongly controlled by temperature and we explored the application of Al- and Ca-in-olivine geothermometers. We demonstrated that these thermometers allow the cooling history of clinopyroxene-poor lithologies to be examined, and that they provide constraints on rates of cooling and emplacement between different tectonic settings. Samples from the fast-spreading Hess Deep record the highest (900–1100 °C) temperatures, followed by the ultraslow-spreading Gakkel and SWIR (700–1000 °C), within which the Tonga harzburgites average at the lower end (700–800 °C). Infiltration of gabbro veins in SWIR peridotites has re-equilibrated these thermometers at ~800 °C. Olivine-based thermometers are thus useful for investigating the thermal histories of peridotites in the 600–1000 °C interval, which is lower than the closure temperature for most pyroxene-based thermometers.
- Group III elements, including Y, Yb, and Ti, are extremely incompatible in olivine. The relative abundances of these elements reflect the extent of partial melting, but our two-stage model demonstrates that their absolute concentrations are diffusively reset by subsolidus re-equilibration. The temperatures predicted based on the extent of subsolidus re-equilibration agrees with thermometry estimates from Group II elements.

Altogether, we found that trace elements in mantle olivine provide a record of processes involved in lithosphere formation, including partial melting, melt–rock interaction, and cooling and subsolidus re-equilibration.

**Supplementary Information** The online version contains supplementary material available at <https://doi.org/10.1007/s00410-023-02044-6>.

**Acknowledgements** The authors acknowledge Kendra J. Lynn and Suzanne Birner for sharing their samples and data. We thank Chin-Chen Kuo and Gerald Poirier for LA-ICPMS support at UD. This research used samples provided by the International Ocean Discovery Program (IODP) from ODP Leg 147, Site 895 (Hess Deep). Subsidius cooling models presented in this study greatly benefited from fruitful discussions on lattice strain models with Emmanuel Codillo and publicly shared files by Chenguang Sun. Thoughtful reviews by Dante Canil, Jason Harvey, and Yan Liang helped strengthen the manuscript substantially and are greatly appreciated. K.-Y. Lin thanks the Department of Earth Sciences and the Graduate College at the University of Delaware for the UD Doctoral fellowship, both of which aided in the completion of this work. Olivine analytical technique development was supported by NSF Grant EAR-1939964 to JMW.

**Data availability** All datasets are included in the electronic supplements.

## Declarations

**Conflict of interest** All authors certify that they have no affiliations with or involvement in any organization or entity with any financial

interest or non-financial interest in the subject matter or materials discussed in this manuscript.

**Open Access** This article is licensed under a Creative Commons Attribution 4.0 International License, which permits use, sharing, adaptation, distribution and reproduction in any medium or format, as long as you give appropriate credit to the original author(s) and the source, provide a link to the Creative Commons licence, and indicate if changes were made. The images or other third party material in this article are included in the article's Creative Commons licence, unless indicated otherwise in a credit line to the material. If material is not included in the article's Creative Commons licence and your intended use is not permitted by statutory regulation or exceeds the permitted use, you will need to obtain permission directly from the copyright holder. To view a copy of this licence, visit <http://creativecommons.org/licenses/by/4.0/>.

## References

- Allen DE, Seyfried WE (2003) Compositional controls on vent fluids from ultramafic-hosted hydrothermal systems at mid-ocean ridges: an experimental study at 400 °C, 500 bars. *Geochim Cosmochim Acta* 67:1531–1542. [https://doi.org/10.1016/S0016-7037\(02\)01173-0](https://doi.org/10.1016/S0016-7037(02)01173-0)
- Anders E, Grevesse N (1989) Abundances of the elements: meteoritic and solar. *Geochim Cosmochim Acta* 53:197–214. [https://doi.org/10.1016/0016-7037\(89\)90286-X](https://doi.org/10.1016/0016-7037(89)90286-X)
- Asimow PD (2002) Steady-state mantle-melt interactions in one dimension: II. Thermal interactions and irreversible terms. *J Petrol* 43:1707–1724. <https://doi.org/10.1093/ptrology/43.9.1707>
- Basch V, Rampone E, Crispini L et al (2018) From mantle peridotites to hybrid troctolites: textural and chemical evolution during melt-rock interaction history (Mt. Maggiore, Corsica, France). *Lithos* 323:4–23. <https://doi.org/10.1016/j.lithos.2018.02.025>
- Basch V, Rampone E, Crispini L et al (2019) Multi-stage reactive formation of troctolites in slow-spreading oceanic lithosphere (Erro-Tobbio, Italy): a combined field and petrochemical study. *J Petrol* 60:873–906. <https://doi.org/10.1093/ptrology/egz019>
- Basch V, Drury MR, Plumper O et al (2021) Intracrystalline melt migration in deformed olivine revealed by trace element compositions and polyphase solid inclusions. *Eur J Mineral* 33:463–477. <https://doi.org/10.5194/ejm-33-463-2021>
- Batanova VG, Thompson JM, Danyushevsky LV et al (2019) New olivine reference material for in situ microanalysis. *Geostandards Geoanal Res*. <https://doi.org/10.1111/ggr.12266>
- Behn MD, Hirth G, Elsenbeck JR (2009) Implications of grain size evolution on the seismic structure of the oceanic upper mantle. *Earth Planet Sci Lett* 282:178–189. <https://doi.org/10.1016/j.epsl.2009.03.014>
- Bevis M, Taylort FW, Schutz BE et al (1995) Geodetic observations of very rapid convergence and back-arc extension at the Tonga arc. *Nature* 374:3
- Birner SK, Warren JM, Cottrell E, Davis FA (2016) Hydrothermal alteration of seafloor peridotites does not influence oxygen fugacity recorded by spinel oxybarometry. *Geology* 44:535–538. <https://doi.org/10.1130/G38113.1>
- Birner SK, Warren JM, Cottrell E et al (2017) Forearc peridotites from Tonga record heterogeneous oxidation of the mantle following subduction initiation. *J Petrol* 58:1755–1780. <https://doi.org/10.1093/ptrology/egx072>
- Birner SK, Cottrell E, Warren JM et al (2018) Peridotites and basalts reveal broad congruence between two independent records of mantle fO<sub>2</sub> despite local redox heterogeneity. *Earth Planet Sci Lett* 494:172–189. <https://doi.org/10.1016/j.epsl.2018.04.035>
- Birner SK, Cottrell E, Warren JM et al (2021) Melt addition to mid-ocean ridge peridotites increases spinel Cr# with no significant effect on recorded oxygen fugacity. *Earth Planet Sci Lett* 566:116951. <https://doi.org/10.1016/j.epsl.2021.116951>
- Bizimis M, Salters VJM, Bonatti E (2000) Trace and REE content of clinopyroxenes from supra-subduction zone peridotites. Implications for melting and enrichment processes in island arcs. *Chem Geol* 165:67–85. [https://doi.org/10.1016/S0009-2541\(99\)00164-3](https://doi.org/10.1016/S0009-2541(99)00164-3)
- Bodinier J-L, Godard M (2014) Orogenic, ophiolitic, and abyssal peridotites. In: *Treatise on geochemistry*. Elsevier, London, pp 103–167
- Brey GP, Köhler T (1990) Geothermobarometry in four-phase lherzolites II. New thermobarometers, and practical assessment of existing thermobarometers. *J Petrol* 31:1353–1378. <https://doi.org/10.1093/ptrology/31.6.1353>
- Byerly BL, Lassiter JC (2014) Isotopically ultradepleted domains in the convecting upper mantle: implications for MORB petrogenesis. *Geology* 42:203–206. <https://doi.org/10.1130/G34757.1>
- Canil D, Fedortchouk Y (2001) Olivine liquid partitioning of Vanadium and other trace elements, with applications to modern and ancient picrites. *Can Mineral* 39:319–330. <https://doi.org/10.2113/gscanmin.39.2.319>
- Canil D, Russell JK (2022) Xenoliths reveal a hot Moho and thin lithosphere at the Cordillera-craton boundary of western Canada. *Geology* 50:1135–1139. <https://doi.org/10.1130/G50151.1>
- Canil D, Russell JK, Fode D (2021) A test of models for recent lithosphere foundering or replacement in the Canadian Cordillera using peridotite xenolith geothermometry. *Lithos* 398–399:106329. <https://doi.org/10.1016/j.lithos.2021.106329>
- Cannat M (1996) How thick is the magmatic crust at slow spreading oceanic ridges? *J Geophys Res* 101:2847–2857. <https://doi.org/10.1029/95JB03116>
- Cannat M, Maia M, Deplus C et al (1995) Thin crust, ultramafic exposures, and rugged faulting patterns at the Mid-Atlantic Ridge (22°–24°N). *Geology* 4:1
- Chen C, De Hoog JCM, Su BX et al (2020) Formation process of dunites and chromitites in Orhaneli and Harmancık ophiolites (NW Turkey): evidence from in-situ Li isotopes and trace elements in olivine. *Lithos*. <https://doi.org/10.1016/j.lithos.2020.105773>
- Cherniak DJ (2010) REE diffusion in olivine. *Am Miner* 95:362–368. <https://doi.org/10.2138/am.2010.3345>
- Cherniak DJ, Liang Y (2007) Rare earth element diffusion in natural enstatite. *Geochim Cosmochim Acta* 71:1324–1340. <https://doi.org/10.1016/j.gca.2006.12.001>
- Cherniak DJ, Liang Y (2014) Titanium diffusion in olivine. *Geochim Cosmochim Acta* 147:43–57. <https://doi.org/10.1016/j.gca.2014.10.016>
- Cherniak DJ, Liang Y (2022) Calcium diffusion in enstatite, with application to closure temperature of the Ca-in-opx thermometer. *Geochim Cosmochim Acta* 332:124–137. <https://doi.org/10.1016/j.gca.2022.06.018>
- Clift PD (1998) Tectonic controls on sedimentation and diagenesis in the Tonga Trench and forearc, southwest Pacific. *Geol Soc Am Bull* 110:483–496
- Constantin M, Hékinian R, Ackermann D, Stoffers P (1995) Mafic and ultramafic intrusions into upper mantle peridotites from fast spreading centers of the Easter Microplate (south east Pacific). In: *Vissers RLM, Nicolas A (eds) Mantle and lower crust exposed in oceanic ridges and in ophiolites*. Springer, Dordrecht, pp 71–120
- Coogan LA (2014) The lower oceanic crust. In: *Treatise on geochemistry*. Elsevier, London, pp 497–541

- Coogan LA, Hain A, Stahl S, Chakraborty S (2005) Experimental determination of the diffusion coefficient for calcium in olivine between 900 and 1500 °C. *Geochim Cosmochim Acta* 69:3683–3694. <https://doi.org/10.1016/j.gca.2005.03.002>
- Coogan LA, Jenkin GRT, Wilson RN (2007) Contrasting cooling rates in the lower oceanic crust at fast- and slow-spreading ridges revealed by geospeedometry. *J Petrol* 48:2211–2231. <https://doi.org/10.1093/ptrology/egm057>
- Coogan LA, Saunders AD, Wilson RN (2014) Aluminum-in-olivine thermometry of primitive basalts: evidence of an anomalously hot mantle source for large igneous provinces. *Chem Geol* 368:1–10. <https://doi.org/10.1016/j.chemgeo.2014.01.004>
- Cramer F, Conrad CP, Montési L, Lithgow-Bertelloni CR (2019) The dynamic life of an oceanic plate. *Tectonophysics* 760:107–135. <https://doi.org/10.1016/j.tecto.2018.03.016>
- D’Errico ME, Warren JM, Godard M (2016) Evidence for chemically heterogeneous Arctic mantle beneath the Gakkel Ridge. *Geochim Cosmochim Acta* 174:291–312. <https://doi.org/10.1016/j.gca.2015.11.017>
- D’Souza RJ, Canil D, Coogan LA (2020) Geobarometry for spinel peridotites using Ca and Al in olivine. *Contrib Mineral Petrol* 175:1–12. <https://doi.org/10.1007/s00410-019-1647-6>
- Dalton CA, Langmuir CH, Gale A (2014) Geophysical and geochemical evidence for deep temperature variations beneath mid-ocean ridges. *Science* 344:80–83. <https://doi.org/10.1126/science.1249466>
- De Hoog JCM, Gall L, Cornell DH (2010) Trace-element geochemistry of mantle olivine and application to mantle petrogenesis and geothermobarometry. *Chem Geol* 270:196–215. <https://doi.org/10.1016/j.chemgeo.2009.11.017>
- Demouchy S, Alard O (2021) Hydrogen, trace, and ultra-trace element distribution in natural olivines. *Contrib Mineral Petrol* 176:26. <https://doi.org/10.1007/s00410-021-01778-5>
- Dick HJB, Bullen T (1984) Chromian spinel as a petrogenetic indicator in abyssal and alpine-type peridotites and spatially associated lavas. *Contrib Mineral Petrol* 86:54–76. <https://doi.org/10.1007/BF00373711>
- Dick HJB, Natland JH (1996) Late-stage melt evolution and transport in the shallow mantle beneath the East Pacific Rise. In: *Proceedings of the ocean drilling program, scientific results*
- Dick HJB, Fisher RL, Bryan WB (1984) Mineralogic variability of the uppermost mantle along mid-ocean ridges. *Earth Planet Sci Lett* 69:88–106. [https://doi.org/10.1016/0012-821X\(84\)90076-1](https://doi.org/10.1016/0012-821X(84)90076-1)
- Dick HJB, Lin J, Schouten H (2003) An ultraslow-spreading class of ocean ridge. *Nature* 426:405–412. <https://doi.org/10.1038/nature02128>
- Dick HJB, Lissenberg CJ, Warren JM (2010) Mantle melting, melt transport, and delivery beneath a slow-spreading ridge: the paleo-MAR from 23 15’N to 23 45’N. *J Petrol* 51:425–467. <https://doi.org/10.1093/ptrology/egp088>
- Dimanov A, Wiedenbeck M (2006) (Fe, Mn)–Mg interdiffusion in natural diopside: effect of pO<sub>2</sub>. *EJM* 18:705–718. <https://doi.org/10.1127/0935-1221/2006/0018-0705>
- Dodson MH (1973) Closure temperature in cooling geochronological and petrological systems. *Contrib Mineral Petrol* 40:259–274. <https://doi.org/10.1007/BF00373790>
- Dohmen R (2002) Si and O diffusion in olivine and implications for characterizing plastic flow in the mantle. *Geophys Res Lett* 29:2030. <https://doi.org/10.1029/2002GL015480>
- Dohmen R, Chakraborty S (2007) Fe–Mg diffusion in olivine II: point defect chemistry, change of diffusion mechanisms and a model for calculation of diffusion coefficients in natural olivine. *Phys Chem Minerals* 34:409–430. <https://doi.org/10.1007/s00269-007-0158-6>
- Drouin M, Godard M, Ildefonse B et al (2009) Geochemical and petrographic evidence for magmatic impregnation in the oceanic lithosphere at Atlantis Massif, Mid-Atlantic Ridge (IODP Hole U1309D, 30°N). *Chem Geol* 264:71–88. <https://doi.org/10.1016/j.chemgeo.2009.02.013>
- Dyger N, Liang Y (2015) Temperatures and cooling rates recorded in REE in coexisting pyroxenes in ophiolitic and abyssal peridotites. *Earth Planet Sci Lett* 420:151–161. <https://doi.org/10.1016/j.epsl.2015.02.042>
- Dyger N, Kelemen PB, Liang Y (2017) Spatial variations in cooling rate in the mantle section of the Samail ophiolite in Oman: implications for formation of lithosphere at mid-ocean ridges. *Earth Planet Sci Lett* 465:134–144. <https://doi.org/10.1016/j.epsl.2017.02.038>
- Ferrando C, Godard M, Ildefonse B, Rampone E (2018) Melt transport and mantle assimilation at Atlantis Massif (IODP Site U1309): constraints from geochemical modeling. *Lithos* 323:24–43. <https://doi.org/10.1016/j.lithos.2018.01.012>
- Fisher RL, Goodwillie AM (1997) The physiography of the Southwest Indian Ridge. *Mar Geophys Res* 19:451–455. <https://doi.org/10.1023/A:1004365019534>
- Foley SF, Prelevic D, Rehfeldt T, Jacob DE (2013) Minor and trace elements in olivines as probes into early igneous and mantle melting processes. *Earth Planet Sci Lett* 363:181–191. <https://doi.org/10.1016/j.epsl.2012.11.025>
- Ganguly J, Tirone M (1999) Diffusion closure temperature and age of a mineral with arbitrary extent of diffusion: theoretical formulation and applications. *Earth Planet Sci Lett* 170:131–140. [https://doi.org/10.1016/S0012-821X\(99\)00089-8](https://doi.org/10.1016/S0012-821X(99)00089-8)
- Gillis K, Mevel C, Allan J (1993) ODP volume 147 initial report. *Proc Ocean Drilling Program*. <https://doi.org/10.2973/odp.proc.ir.147.1993>
- Gleeson MLM, Lissenberg CJ, Antoshechkina PM (2023) Porosity evolution of mafic crystal mush during reactive flow. *Nat Commun* 14:3088. <https://doi.org/10.1038/s41467-023-38136-x>
- Grambling NL, Dyger N, Boring B et al (2022) Thermal history of lithosphere formed beneath fast spreading ridges: constraints from the mantle transition zone of the East Pacific Rise at Hess Deep and Oman Drilling Project, Wadi Zeeb, Samail Ophiolite. *JGR Solid Earth*. <https://doi.org/10.1029/2021JB022696>
- Grindlay NR, Madsen JA, Rommevaux-Jestin C, Sclater J (1998) A different pattern of ridge segmentation and mantle Bouguer gravity anomalies along the ultra-slow spreading Southwest Indian Ridge (15°30’E to 25°E). *Earth Planet Sci Lett* 11:1
- Hellebrand E, Snow JE, Dick HJB, Hofmann AW (2001) Coupled major and trace elements as indicators of the extent of melting in mid-ocean-ridge peridotites. *Nature* 410:677–681. <https://doi.org/10.1038/35070546>
- Hellebrand E, Snow JE, Mostefaoui S, Hoppe P (2005) Trace element distribution between orthopyroxene and clinopyroxene in peridotites from the Gakkel Ridge: a SIMS and NanoSIMS study. *Contrib Mineral Petrol* 150:486–504. <https://doi.org/10.1007/s00410-005-0036-5>
- Hirth G, Kohlstedt DL (1996) Water in the oceanic upper mantle: implications for rheology, melt extraction and the evolution of the lithosphere. *Earth Planet Sci Lett* 144:93–108
- Jochum KP, Dingwell DB, Rocholl A et al (2000) The preparation and preliminary characterisation of eight geological MPI-DING reference glasses for in-situ microanalysis. *Geostand Geoanal Res* 24:87–133. <https://doi.org/10.1111/j.1751-908X.2000.tb00590.x>
- Jochum KP, Nohl U, Herwig K et al (2005a) Georem: a new geochemical database for reference materials and isotopic standards. *Geostand Geoanal Res* 29:333–338. <https://doi.org/10.1111/j.1751-908X.2005.tb00904.x>
- Jochum KP, Willbold M, Raczek I et al (2005b) Chemical characterisation of the USGS reference glasses GSA-1G, GSC-1G, GSD-1G, GSE-1G, BCR-2G, BHVO-2G and BIR-1G using EPMA, ID-TIMS, ID-ICP-MS and LA-ICP-MS. *Geostand Geoanal Res*

- 29:285–302. <https://doi.org/10.1111/j.1751-908X.2005.tb00901.x>
- Jochum KP, Weis U, Schwager B et al (2016) Reference values following ISO guidelines for frequently requested rock reference materials. *Geostand Geoanal Res* 40:333–350. <https://doi.org/10.1111/j.1751-908X.2015.00392.x>
- Johnson KT, Dick HJB, Shimizu N (1990) Melting in the oceanic upper mantle: an ion microprobe study of diopsides in abyssal peridotites. *J Geophys Res* 95:2661–2678
- Karson JA, Klein EM, Hurst SD et al (2002) Structure of uppermost fast-spread oceanic crust exposed at the Hess Deep Rift: implications for subaxial processes at the East Pacific Rise. *Geochem Geophys Geosyst*. <https://doi.org/10.1029/2001GC000155>
- Katz RF, Jones DWR, Rudge JF, Keller T (2022) Physics of melt extraction from the mantle: speed and style. *Annu Rev Earth Planet Sci* 50:507–540. <https://doi.org/10.1146/annurev-earth-032320-083704>
- Kelemen PB, Shimizu N, Salters VJM (1995) Extraction of mid-ocean-ridge basalt from the upwelling mantle by focused flow of melt in dunite channels. *Nature* 375:747–753. <https://doi.org/10.1038/375747a0>
- Klein EM, Langmuir CH (1987) Global correlations of ocean ridge basalt chemistry with axial depth and crustal thickness. *J Geophys Res* 92:8089. <https://doi.org/10.1029/JB092iB08p08089>
- Lassiter JC, Byerly BL, Snow JE, Hellebrand E (2014) Constraints from Os-isotope variations on the origin of Lena Trough abyssal peridotites and implications for the composition and evolution of the depleted upper mantle. *Earth Planet Sci Lett* 403:178–187. <https://doi.org/10.1016/j.epsl.2014.05.033>
- Le Maitre RW, Streckeis A, Zanettin B et al (2002) *Igneous rocks: a classification and glossary of terms*. Cambridge University Press, Cambridge
- Li J, Kornprobst J, Vielzeuf D, Fabriès J (1995) An improved experimental calibration of the olivine-spinel geothermometer. *Chin J Geochem* 14:68–77. <https://doi.org/10.1007/BF02840385>
- Liang Y (2015) A simple model for closure temperature of a trace element in cooling bi-mineralic systems. *Geochim Cosmochim Acta* 165:35–43. <https://doi.org/10.1016/j.gca.2015.05.028>
- Liang Y, Sun C, Yao L (2013) A REE-in-two-pyroxene thermometer for mafic and ultramafic rocks. *Geochim Cosmochim Acta* 102:246–260. <https://doi.org/10.1016/j.gca.2012.10.035>
- Liang Y, Ji Z, Liu B (2021) What can we learn from REE abundances in clinopyroxene and orthopyroxene in residual mantle peridotites? *Contrib Mineral Petrol* 176:24. <https://doi.org/10.1007/s00410-021-01780-x>
- Liermann H-P, Ganguly J (2002) Diffusion kinetics of Fe<sup>2+</sup> and Mg in aluminous spinel. *Geochim Cosmochim Acta* 66:2903–2913. [https://doi.org/10.1016/S0016-7037\(02\)00875-X](https://doi.org/10.1016/S0016-7037(02)00875-X)
- Lissenberg CJ, Dick HJB (2008) Melt–rock reaction in the lower oceanic crust and its implications for the genesis of mid-ocean ridge basalt. *Earth Planet Sci Lett* 271:311–325. <https://doi.org/10.1016/j.epsl.2008.04.023>
- Lissenberg CJ, MacLeod CJ (2016) A reactive porous flow control on mid-ocean ridge magmatic evolution. *J Petrol* 57:2195–2220. <https://doi.org/10.1093/ptrology/egw074>
- Liu C, Li J, Tao C et al (2020) Variations in faulting style of the Southwest Indian Ridge (46°–53.5°E): Implications for crustal accretion process at ultraslow-spreading ridges. *Tectonophysics* 790:228552. <https://doi.org/10.1016/j.tecto.2020.228552>
- Lonsdale P (1988) Structural pattern of the Galapagos microplate and evolution of the Galapagos triple junctions. *J Geophys Res* 93:13551–13574. <https://doi.org/10.1029/JB093iB11p13551>
- Lynn KJ, Cottrell E, Warren JM et al (2018) An oxidized signature for the Gakkel Ridge “dupal-like” isotopic composition. In: AGU fall meeting
- Mallmann G, O’Neill HSTC, Klemme S (2009) Heterogeneous distribution of phosphorus in olivine from otherwise well-equilibrated spinel peridotite xenoliths and its implications for the mantle geochemistry of lithium. *Contrib Mineral Petrol* 158:485–504. <https://doi.org/10.1007/s00410-009-0393-6>
- Manning CE, MacLeod CJ (1996) Fracture-controlled metamorphism of Hess Deep Gabbros, Site 894: constraints on the roots of mid-ocean-ridge hydrothermal systems at fast-spreading centers. In: *Proceedings of the ocean drilling program, 147 scientific results*. Ocean Drilling Program
- Manning CE, MacLeod CJ, Weston PE (2000) Lower-crustal cracking front at fast-spreading ridges: evidence from the East Pacific Rise and the Oman Ophiolite. In: *Ophiolites and oceanic crust: new insights from field studies and the ocean drilling program*. Geological Society of America
- Mendel V, Sauter D, Parson L, Vanney J-R (1997) Segmentation and morphotectonic variations along a super slow-spreading center: the Southwest Indian Ridge (57°E–70°E). *Mar Geophys Res* 19:505–533. <https://doi.org/10.1023/A:1004232506333>
- Michael PJ, Langmuir CH, Dick HJB et al (2003) Magmatic and amalgamated seafloor generation at the ultraslow-spreading Gakkel ridge, Arctic Ocean. *Nature* 423:956–961. <https://doi.org/10.1038/nature01704>
- Müller T, Dohmen R, Becker HW et al (2013) Fe–Mg interdiffusion rates in clinopyroxene: experimental data and implications for Fe–Mg exchange geothermometers. *Contrib Mineral Petrol* 166:1563–1576. <https://doi.org/10.1007/s00410-013-0941-y>
- Naif S (2018) An upper bound on the electrical conductivity of hydrated oceanic mantle at the onset of dehydration melting. *Earth Planet Sci Lett* 482:357–366. <https://doi.org/10.1016/j.epsl.2017.11.024>
- Neave DA, Shorttle O, Oeser M et al (2018) Mantle-derived trace element variability in olivines and their melt inclusions. *Earth Planet Sci Lett* 483:90–104. <https://doi.org/10.1016/j.epsl.2017.12.014>
- Niu Y (2004) Bulk-rock major and trace element compositions of abyssal peridotites: implications for mantle melting, melt extraction and post-melting processes beneath Mid-Ocean ridges. *J Petrol* 45:2423–2458. <https://doi.org/10.1093/ptrology/egh068>
- Niu Y, Langmuir CH, Kinzler RJ (1997) The origin of abyssal peridotites: a new perspective. *Earth Planet Sci Lett* 152:251–265. [https://doi.org/10.1016/S0012-821X\(97\)00119-2](https://doi.org/10.1016/S0012-821X(97)00119-2)
- Ozawa K (1983) Evaluation of olivine-spinel geothermometry as an indicator of thermal history for peridotites. *Contrib Mineral Petrol* 82:52–65. <https://doi.org/10.1007/BF00371175>
- Patriat P, Sauter D, Munsch M, Parson L (1997) A survey of the Southwest Indian Ridge axis between Atlantis II Fracture Zone and the Indian Ocean Triple Junction: regional setting and large scale segmentation. *Mar Geophys Res* 19:457–480
- Patterson SN, Lynn KJ, Prigent C, Warren JM (2021) High temperature hydrothermal alteration and amphibole formation in Gakkel Ridge abyssal peridotites. *Lithos* 392–393:106107. <https://doi.org/10.1016/j.lithos.2021.106107>
- Quinn DP, Saleeby JB, Ducea MN et al (2018) Late cretaceous construction of the mantle lithosphere beneath the central California coast revealed by crystal knob xenoliths. *Geochem Geophys Geosyst* 19:3302–3346. <https://doi.org/10.1029/2017GC007260>
- Rampone E, Borghini G, Godard M et al (2016) Melt/rock reaction at oceanic peridotite/gabbro transition as revealed by trace element chemistry of olivine. *Geochim Cosmochim Acta* 190:309–331. <https://doi.org/10.1016/j.gca.2016.06.029>
- Reagan MK, Ishizuka O, Stern RJ et al (2010) Fore-arc basalts and subduction initiation in the Izu-Bonin-Mariana system. *Geochem Geophys Geosyst*. <https://doi.org/10.1029/2009GC002871>

- Rooney T, Girard G, Tappe S (2020) The impact on mantle olivine resulting from carbonated silicate melt interaction. *Contrib Mineral Petrol* 175:1–15. <https://doi.org/10.1007/s00410-020-01694-0>
- Ryan WBF, Carbotte SM, Coplan JO et al (2009) Global multi-resolution topography synthesis. *Geochem Geophys Geosyst*. <https://doi.org/10.1029/2008GC002332>
- Salters VJM, Dick HJB (2002) Mineralogy of the mid-ocean-ridge basalt source from neodymium isotopic composition of abyssal peridotites. *Nature* 418:68–72. <https://doi.org/10.1038/nature00798>
- Sanfilippo A, Tribuzio R, Tiepolo M (2014) Mantle–crust interactions in the oceanic lithosphere: constraints from minor and trace elements in olivine. *Geochim Cosmochim Acta* 141:423–439. <https://doi.org/10.1016/j.gca.2014.06.012>
- Sanfilippo A, Tribuzio R, Ottolini L, Hamada M (2017) Water, lithium and trace element compositions of olivine from Lanzo South replacive mantle dunites (Western Alps): new constraints into melt migration processes at cold thermal regimes. *Geochim Cosmochim Acta* 214:51–72. <https://doi.org/10.1016/j.gca.2017.07.034>
- Sauter D, Cannat M, Rouméjon S et al (2013) Continuous exhumation of mantle-derived rocks at the Southwest Indian Ridge for 11 million years. *Nat Geosci* 6:314–320. <https://doi.org/10.1038/ngeo1771>
- Secchiari A, Montanini A, Cluzel D (2022) Temperatures and cooling rates recorded by the new caledonia ophiolite: implications for cooling mechanisms in young forearc sequences. *Geochem Geophys Geosyst*. <https://doi.org/10.1029/2021GC009859>
- Seyler M, Brunelli D (2018) Sodium-chromium covariation in residual clinopyroxenes from abyssal peridotites sampled in the 43°–46°E region of the Southwest Indian Ridge. *Lithos* 302–303:142–157. <https://doi.org/10.1016/j.lithos.2017.12.018>
- Seyler M, Toplis MJ, Lorand J-P et al (2001) Clinopyroxene microtextures reveal incompletely extracted melts in abyssal peridotites. *Geology* 29:155–158
- Shaw DM (1970) Trace element fractionation during anatexis. *Geochimica et Cosmochimica Acta* 34(2):237–243
- Shejwalkar A, Coogan LA (2013) Experimental calibration of the roles of temperature and composition in the Ca-in-olivine geothermometer at 0.1 MPa. *Lithos* 177:54–60. <https://doi.org/10.1016/j.lithos.2013.06.013>
- Smith DK, Schouten H (2018) Opening of hess deep rift at the galapagos triple junction. *Geophys Res Lett* 45:3942–3950. <https://doi.org/10.1029/2018GL077555>
- Smith DK, Schouten H, Parnell-Turner R et al (2020) The evolution of seafloor spreading behind the tip of the westward propagating Cocos-Nazca spreading center. *Geochem Geophys Geosyst*. <https://doi.org/10.1029/2020GC008957>
- Sobolev AV, Hofmann AW, Kuzmin DV et al (2007) The amount of recycled crust in sources of mantle-derived melts. *Science* 316:7
- Spandler C, O'Neill HSTC (2010) Diffusion and partition coefficients of minor and trace elements in San Carlos olivine at 1300 °C with some geochemical implications. *Contrib Mineral Petrol* 159:791–818. <https://doi.org/10.1007/s00410-009-0456-8>
- Standish JJ, Dick HJB, Michael PJ et al (2008) MORB generation beneath the ultraslow spreading Southwest Indian Ridge (9–25°E): major element chemistry and the importance of process versus source: SWIR MORB-PROCESS VERSUS SOURCE. *Geochem Geophys Geosyst*. <https://doi.org/10.1029/2008GC001959>
- Stern RJ, Gerya T (2018) Subduction initiation in nature and models: a review. *Tectonophysics* 746:173–198. <https://doi.org/10.1016/j.tecto.2017.10.014>
- Stracke A (2012) Earth's heterogeneous mantle: a product of convection-driven interaction between crust and mantle. *Chem Geol* 330–331:274–299. <https://doi.org/10.1016/j.chemgeo.2012.08.007>
- Su B, Chen Y, Mao Q et al (2019) Minor elements in olivine inspect the petrogenesis of orogenic peridotites. *Lithos* 344–345:207–216. <https://doi.org/10.1016/j.lithos.2019.06.029>
- Sun C, Liang Y (2012) Distribution of REE between clinopyroxene and basaltic melt along a mantle adiabat: effects of major element composition, water, and temperature. *Contrib Mineral Petrol* 163:807–823. <https://doi.org/10.1007/s00410-011-0700-x>
- Sun C, Liang Y (2013a) The importance of crystal chemistry on REE partitioning between mantle minerals (garnet, clinopyroxene, orthopyroxene, and olivine) and basaltic melts. *Chem Geol* 358:23–36. <https://doi.org/10.1016/j.chemgeo.2013.08.045>
- Sun C, Liang Y (2013b) Distribution of REE and HFSE between low-Ca pyroxene and lunar picritic melts around multiple saturation points. *Geochim Cosmochim Acta* 119:340–358. <https://doi.org/10.1016/j.gca.2013.05.036>
- Sun C, Liang Y (2014) An assessment of subsolidus re-equilibration on REE distribution among mantle minerals olivine, orthopyroxene, clinopyroxene, and garnet in peridotites. *Chem Geol* 372:80–91. <https://doi.org/10.1016/j.chemgeo.2014.02.014>
- Tappins DR, Bruns TRL, Geist EL (1994) Rifting of the Tonga/Lau Ridge and formation of the Lau backarc basin: evidence from site 840 on the Tonga Ridge. In: Proceedings of the ocean drilling program, 135 scientific results. Ocean Drilling Program
- Van Orman JA, Grove TL, Shimizu N (2001) Rare earth element diffusion in diopside: influence of temperature, pressure, and ionic radius, and an elastic model for diffusion in silicates. *Contrib Mineral Petrol* 141:687–703. <https://doi.org/10.1007/s0041001001269>
- Vogt PR, Taylor PT, Kovacs LC, Johnson GL (1979) Detailed aeromagnetic investigation of the Arctic Basin. *J Geophys Res* 84:1071. <https://doi.org/10.1029/JB084iB03p01071>
- Voigt M, von der Handt A (2011) Influence of subsolidus processes on the chromium number in spinel in ultramafic rocks. *Contrib Mineral Petrol* 162:675–689. <https://doi.org/10.1007/s00410-011-0618-3>
- Wan Z, Coogan LA, Canil D (2008) Experimental calibration of aluminum partitioning between olivine and spinel as a geothermometer. *Am Miner* 93:1142–1147. <https://doi.org/10.2138/am.2008.2758>
- Wang J, Su BX, Robinson PT et al (2021) Trace elements in olivine: proxies for petrogenesis, mineralization and discrimination of mafic-ultramafic rocks. *Lithos*. <https://doi.org/10.1016/j.lithos.2021.106085>
- Warren JM (2007) Geochemical and rheological constraints on the dynamics of the oceanic upper mantle. PhD thesis. MIT/WHOI Joint Program
- Warren JM (2016) Global variations in abyssal peridotite compositions. *Lithos* 248–251:193–219. <https://doi.org/10.1016/j.lithos.2015.12.023>
- Warren JM, Shimizu N (2010) Cryptic variations in abyssal peridotite compositions: evidence for shallow-level melt infiltration in the oceanic lithosphere. *J Petrol* 51:395–423. <https://doi.org/10.1093/petrology/egp096>
- Warren JM, Shimizu N, Sakaguchi C et al (2009) An assessment of upper mantle heterogeneity based on abyssal peridotite isotopic compositions. *J Geophys Res* 114:B12203. <https://doi.org/10.1029/2008JB006186>
- Wasylenki LE (2003) Near-solidus melting of the shallow upper mantle: partial melting experiments on depleted peridotite. *J Petrol* 44:1163–1191. <https://doi.org/10.1093/petrology/44.7.1163>

- Witt-Eickschen G, O'Neill HSTC (2005) The effect of temperature on the equilibrium distribution of trace elements between clinopyroxene, orthopyroxene, olivine and spinel in upper mantle peridotite. *Chem Geol* 221:65–101. <https://doi.org/10.1016/j.chemgeo.2005.04.005>
- Witt-Eickschen G, Palme H, O'Neill HSTC, Allen CM (2009) The geochemistry of the volatile trace elements As, Cd, Ga, In and Sn in the Earth's mantle: new evidence from in situ analyses of mantle xenoliths. *Geochim Cosmochim Acta* 73:1755–1778. <https://doi.org/10.1016/j.gca.2008.12.013>
- Workman RK, Hart SR (2005) Major and trace element composition of the depleted MORB mantle (DMM). *Earth Planet Sci Lett* 231:53–72. <https://doi.org/10.1016/j.epsl.2004.12.005>
- Yao L, Liang Y (2015) Closure temperature in cooling bi-mineralic systems: I. Definition and with application to REE-in-two-pyroxene thermometer. *Geochim Cosmochim Acta* 162:137–150. <https://doi.org/10.1016/j.gca.2015.03.041>
- Yao L, Sun C, Liang Y (2012) A parameterized model for REE distribution between low-Ca pyroxene and basaltic melts with applications to REE partitioning in low-Ca pyroxene along a mantle adiabat and during pyroxenite-derived melt and peridotite interaction. *Contrib Mineral Petrol* 164:261–280. <https://doi.org/10.1007/s00410-012-0737-5>
- Zhang W-Q, Dick HJB, Liu C-Z et al (2021) MORB melt transport through atlantis bank oceanic batholith (SW Indian Ridge). *J Petrol* 62:egab034. <https://doi.org/10.1093/petrology/egab034>
- Zhukova I, O'Neill H, Campbell IH (2017) A subsidiary fast-diffusing substitution mechanism of Al in forsterite investigated using diffusion experiments under controlled thermodynamic conditions. *Contrib Mineral Petrol* 172:53. <https://doi.org/10.1007/s00410-017-1365-x>

**Publisher's Note** Springer Nature remains neutral with regard to jurisdictional claims in published maps and institutional affiliations.